How to cite: *Angew. Chem. Int. Ed.* **2023,** *62,* e202217565
International Edition: doi.org/10.1002/anie.202217565
German Edition: doi.org/10.1002/ange.202217565

Metal-Organic Frameworks

Metal-Organic Frameworks for Photocatalytic Water Splitting and CO_2 Reduction

*Kang Sun, Yunyang Qian, and Hai-Long Jiang**

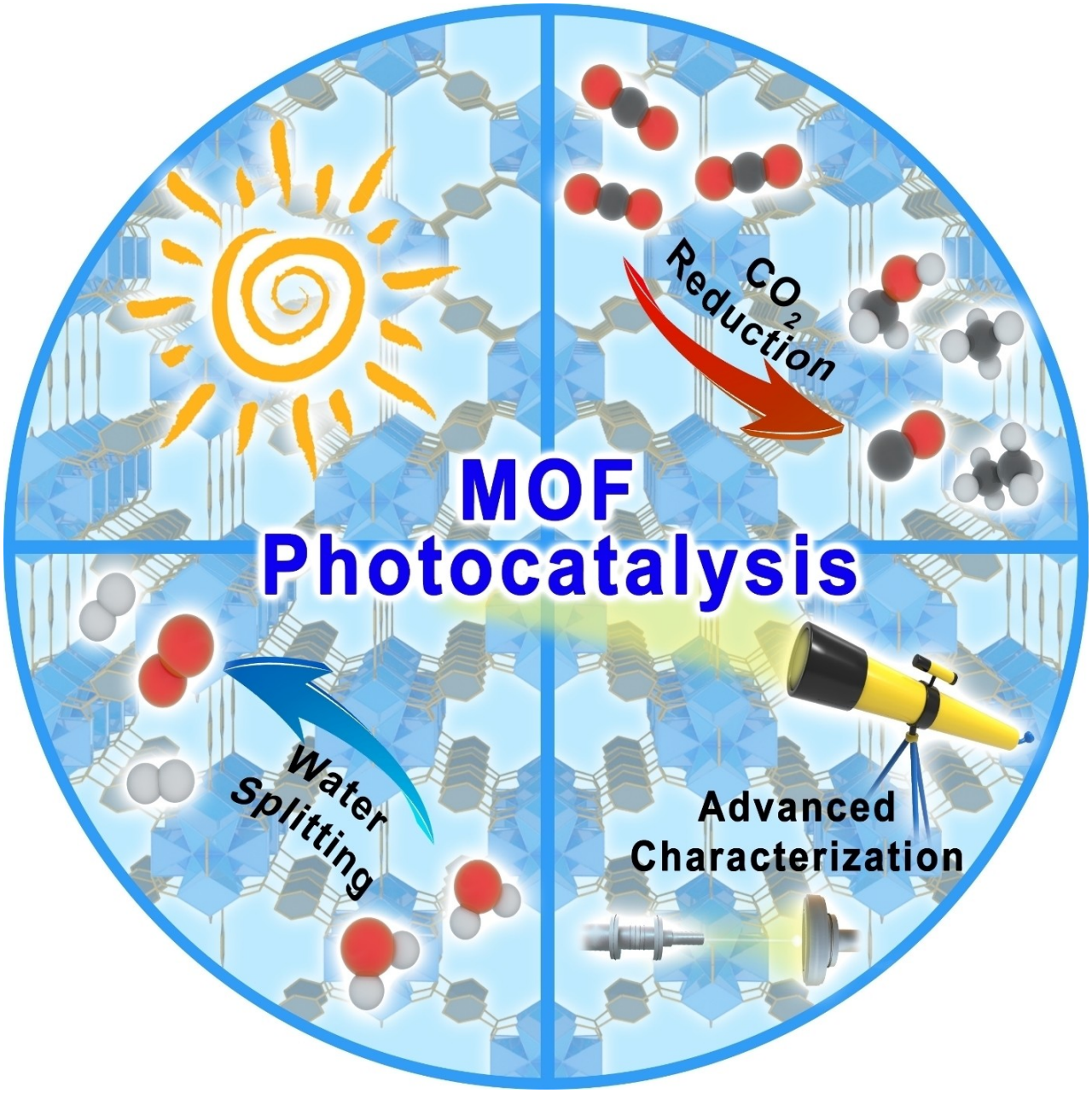

Abstract: Photocatalytic water splitting and carbon dioxide (CO_2) reduction provide promising solutions to global energy and environmental issues. In recent years, metal-organic frameworks (MOFs), a class of crystalline porous solids featuring well-defined and tailorable structures as well as high surface areas, have captured great interest toward photocatalytic water splitting and CO_2 reduction. In this review, the semiconductor-like behavior of MOFs is first discussed. We then summarize the recent advances in photocatalytic water splitting and CO_2 reduction over MOF-based materials and focus on the unique advantage of MOFs for clarifying the structure-property relationship in photocatalysis. In addition, some representative characterization techniques have been presented to unveil the photocatalytic kinetics and reaction intermediates in MOF-based systems. Finally, the challenges, and perspectives for future directions are proposed.

1. Introduction

Fossil fuels, such as coal, oil, and natural gas, serve approximately 80 % of human energy requirements. Unfortunately, fossil fuels are a nonrenewable resource and inhomogeneous distribution in region, while responsible for the excessive emission of CO_2, SO_2, NO_x, particulate pollutants, etc. Among the various emissions, CO_2 causes a severe greenhouse effect, which has become one of the greatest threats to the sustainable development of mankind. In a word, the overreliance on fossil fuels has led to the serious energy crisis and greenhouse effect that the world is facing today. There is a global consensus to pursue sustainable and renewable energies and reduce atmospheric CO_2. In the past decade, great efforts have been devoted to developing various approaches toward sustainable energies, including solar energy, wind energy, nuclear energy, etc.[1]

Solar energy is the most abundant energy source in nature, and is capable of supplying more than a thousand times the total world energy consumption. However, solar energy is diffuse and intermittent, making it very difficult to apply directly. There is a demand to convert solar energy into usable and storable chemical energy. In natural photosynthesis, plants can harvest solar energy to produce biomass from H_2O and CO_2. Inspired by this, scientists proposed artificial photosynthesis to mimic natural photosynthesis. In 2010, the US Department of Energy (DOE) established the Joint Center for Artificial Photosynthesis (JCAP) with the goal of producing H_2 and carbon-based fuels from CO_2 and H_2O via solar energy.[2] H_2 is an ideal zero-emission fuel that can be used to produce fuel and electricity with water only as the combustion product. Meanwhile, the conversion of CO_2 into fuels will help to achieve a sustainable carbon cycle and alleviate the critical greenhouse effect.[3]

Artificial photosynthesis usually proceeds in the following steps (Figure 1): **Step 1**: A photocatalyst absorbs photons with an energy higher than its band gap to generate electron-hole pairs. **Step 2**: The electron-hole pairs are separated and migrate to the surface of photocatalysts. **Step 3**: The photogenerated carriers drive redox reactions.[4] Photocatalysts, including homogeneous and heterogeneous systems, are at the core of artificial photosynthesis. Homogenous photocatalysts are mainly molecular materials with well-defined and easily modified structures.[5] They are good candidates to investigate the structure-property relationships in photocatalysis. However, homogeneous catalysts and reactants are soluble and uniformly mixed, which gives rise to technical difficulties in catalyst cycling and economic disadvantages. For heterogeneous photocatalytic systems, catalysts and reaction species exist in different physical phases, which can be easily reused and meet industrial needs.[6] Nevertheless, the structural control of traditional heterogeneous catalysts at the atomic level, and accordingly the precise investigation of related reaction mechanisms is usually challenging. As an alternative, a class of crystalline porous materials, metal-organic frameworks (MOFs) constructed by metal ions/clusters and organic linkers, feature atomically precise and tailorable structures as well as unique physicochemical properties,[7] bridging the gap between heterogeneous and homogeneous catalysts.[8] MOFs have emerged as excellent photocatalysts in photocatalytic water splitting and CO_2 reduction in recent years.[9]

In this review, we first clarify the fundamentals, e.g. semiconductor-like behavior and merits, of MOFs toward photocatalysis in **Section 2**. Given that some excellent reviews on photocatalytic water splitting and CO_2 reduction over MOFs have been published over the past decade,[9] we provide an overview of recent developments in MOF photo-

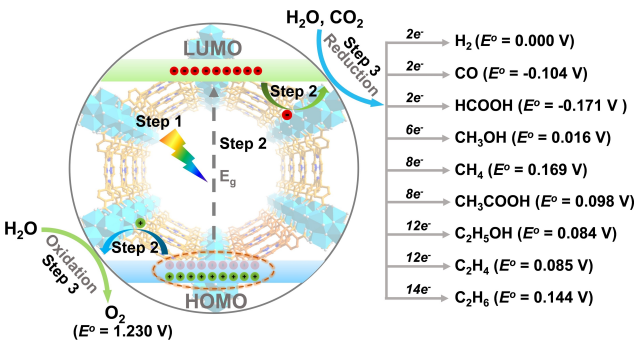

Figure 1. Schematic diagrams of the three steps within a photocatalytic reaction and various potentials for typical water splitting and carbon dioxide reduction (V vs. RHE, pH = 0).

[*] K. Sun, Y. Qian, Prof. Dr. H.-L. Jiang
Department of Chemistry, Collaborative Innovation Center of Chemistry for Energy Materials (iChEM), University of Science and Technology of China
Hefei, Anhui 230026 (P. R. China)
E-mail: jianglab@ustc.edu.cn
Homepage: http://mof.ustc.edu.cn/

catalytic water splitting and CO_2 reduction with a focus on understanding the structure-property relationship in photocatalysis in **Sections 3** and **4**. In addition, typical space- and time-resolved characterization techniques to investigate the kinetic behavior in MOF-based photocatalysis, and techniques for tracing reaction intermediates and charge transfer are discussed in **Section 5**. Finally, the challenges and further opportunities of MOFs for water splitting and CO_2 reduction are envisioned.

2. Fundamentals of MOFs for Photocatalysis

2.1. The Semiconductor-like Behavior of MOFs

Although recent publications related to MOF photocatalysis are increasing geometrically in recent years, the issue regarding MOFs as semiconductors or molecular entities assembled in a periodic fashion remains highly controversial. From the definition of semiconductors, early-stage studies on semiconductors can be traced back to the 19th century, when semiconductors were defined as materials with conductivity lying between metals and insulators.[10] In terms of conductivity, most MOFs should be considered as molecular aggregates due to their poor conductivity. However, with the development of theory and application scenarios, many materials with poor conductivity, such as TiO_2, ZnO, diamond, etc., are defined as semiconductors.[11] Therefore, it might not be accurate to tie together the question of whether MOFs are semiconductors with conductivity.

Currently, it is generally accepted that there are three features for semiconductors: 1) their conductivity increases with increasing temperature; 2) doping can change their conductivity; and 3) photoconductivity, that is, semiconductors can produce carriers under light.[10] In a very early work, García, Corma and co-workers compared the photoinduced charge separation behavior of MOFs with that of zeolites, supporting the conclusion that MOFs are semiconductors.[12] Xu et al. provided clear electron paramagnetic resonance (EPR) evidence on the photogenerated electrons and holes located on the Zr-oxo cluster and the linker of PCN-222, respectively, which further supports the charge transfer behavior of MOFs.[13] Band bending is an important semiconducting behavior that causes the driving force for interfacial charge transfer in semiconductor composites.[6d] Recently, the band bending behavior in MOFs was demonstrated by surface photovoltage (SPV) spectra by the Jiang group.[14] A representative MOF, MIL-125-NH_2, was integrated with the metal oxides of MoO_3 and V_2O_5 to obtain MoO_3/MIL-125-NH_2 and V_2O_5/MIL-125-NH_2, respectively. The energy level difference drove electrons to migrate from the highest occupied molecular orbital (HOMO) of the MOF to the conduction band minimum (CBM) of the metal oxides (Figure 2a), resulting in upward band bending and much enhanced photocatalysis. To rationalize this, the SPV signals were collected. Compared with the parent MOF, both composites displayed significantly stronger SPV signals (Figure 2b), manifesting the increment of the hole accumulation concentration on the MOF surface. This work unveils the band bending behavior of MOFs, which is characteristic of classical semiconductors based on band theory.

In addition, according to the IUPAC recommended terms in photocatalysis, a semiconductor is a material whose electrical conductivity (κ) increases exponentially with increasing temperature, obeying Van't-Hoff's law:[15]

Kang Sun received his B.S. degree (2017) in chemistry from Yunnan University. He is currently a Ph.D. student under the guidance of Prof. Hai-Long Jiang at University of Science and Technology of China (USTC). His research focuses on the development of MOF-based materials for photocatalysis.

Yunyang Qian received his B.S. degree (2017) from China University of Petroleum. He is presently a Ph.D. student under the guidance of Prof. Hai-Long Jiang at USTC. His work is associated with the development of photocatalysts based on covalent organic framework-based materials.

Hai-Long Jiang earned his Ph.D. (2008) from Chinese Academy of Sciences. He subsequently worked at the National Institute of Advanced Industrial Science and Technology (Japan) during 2008–2011. After a postdoctoral stint at Texas A&M University (USA), he became a full professor at USTC in 2013. He was elected a Fellow of the Royal Society of Chemistry (FRSC) in 2018. His research interest currently lies in biomimetic microenvironment modulation (MEM) of catalytic centers based on crystalline porous materials (particularly MOFs).

$$\kappa = \kappa_0 e^{\frac{-\Delta H}{RT}}$$

where ΔH is the enthalpy of conduction, R is the molar gas constant, and T is the temperature. Following this definition, some other results from previous reports support the semiconducting nature of MOFs.[16] Regarding semiconducting properties and the definition of IUPAC, MOFs could indeed be considered as a kind of semiconductor; or at least, MOFs possess semiconductor-like behaviors, as evidenced by many experiments.

On the other hand, the well-accepted charge transfer process, such as linker-to-metal charge transfer (LMCT), in MOFs reveals their localized band structures, suggesting that MOFs are more likely molecular catalysts rather than classical semiconductors.[9a,17] Meanwhile, it is worth noting that there are even sporadic contradictory cases between theory and experiment. For example, the LMCT process is adopted to explain the charge transfer process of UiO-66, as also evidenced by EPR spectra.[18] However, theoretical calculations prove that both the HOMO and the lowest unoccupied molecular orbital (LUMO) of UiO-66 are localized in the linker,[19] that is, the linker-to-linker charge transfer (LLCT) process should occur to UiO-66. Taken together, some theoretical uncertainties remain to be addressed, and further efforts are required to understand the more likely dual nature of MOFs compared with classical semiconductors and molecular catalysts.[20]

2.2. The Merits of MOF Photocatalysts

As an emerging class of photocatalysts, MOFs have many unique advantages compared with semiconductor photocatalysts. First, the diversified organic linkers and metal nodes as well as the reticular nature of MOFs enable the high programmability of their structures. By altering or furnishing the organic linkers and metal nodes, the photosensitivity range can be extended from ultraviolet to visible and even to infrared light.[21] In addition, the HOMO and LUMO positions can be directionally regulated, thereby influencing the redox ability of MOFs and controlling the reaction selectivity.[22] Moreover, the MOF structure is highly compatible, which facilitates the incorporation of different guest species or integration with diverse substances.[8,9,23] The photosensitizers or active sites can be flexibly immobilized by the MOF skeleton or encapsulated into the MOF pore space. Second, the structural defects in photocatalysts act as electron-hole recombination centers, mostly leading to negative photocatalytic performance.[6b] The perfect crystal structure with fewer defects in MOFs would be beneficial to suppress the recombination of electrons and holes.[9b–d] Third, the porous structure and large surface area of MOFs present significant advantages, providing more exposed active sites and substrate transport channels in photocatalysis, compared with other photocatalysts. Especially, the porosity is favorable to the timely redox reaction of charge carriers with substrates, thereby reducing the charge diffusion distance and suppressing the bulk recombination of electrons and holes. Based on Mie scattering theory, the interior cavity of hollow nanostructure can greatly enhance light harvesting by multiple reflection and scattering.[24] Similarly, it was evidenced that MOFs can enhance the light absorption in solar cells, which is likely due to the multiple reflection and scattering of light in the porous pocket of MOFs.[25] Furthermore, as porous materials, the density of MOFs is much lower than that of conventional inorganic semiconductors, facilitating lightweight devices, and practical large-scale applications.[26] Finally, the well-defined and tailorable structural features of MOFs make them an ideal platform for understanding the structure-activity relationship.

3. Photocatalytic Water Splitting

3.1. The Brief Mechanism

Photocatalytic water splitting consists of two half-reactions, known as the oxygen evolution reaction (OER) and H_2 production (also called hydrogen evolution reaction, HER). It is an uphill reaction that should overcome an energy barrier of 1.23 eV. To achieve overall water splitting, in principle, the band gap energy (E_g) of MOFs should be >1.23 eV to meet the thermodynamic requirement, and the LUMO (also called CBM) and HOMO (also called valence

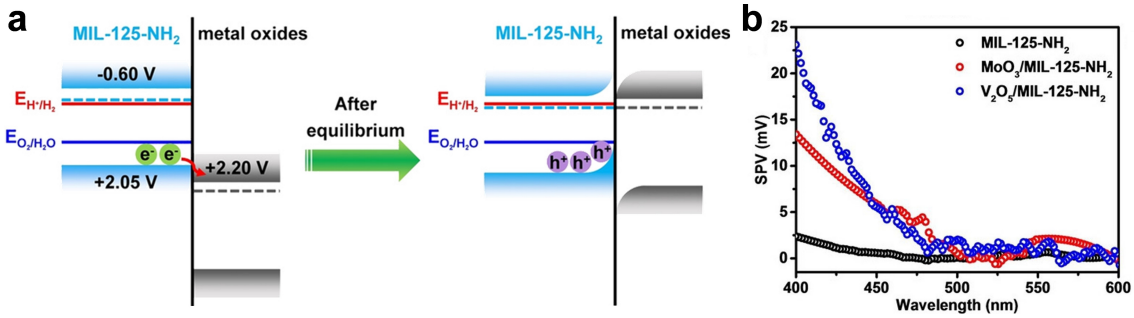

Figure 2. (a) Schematic mechanism for band bending and built-in electric field formation, as well as related energy levels of both components in the MOF composites. (b) SPV spectra of MIL-125-NH_2, MoO_3/MIL-125-NH_2, and V_2O_5/MIL-125-NH_2. Adapted with permission.[14] Copyright 2022, Wiley-VCH.

band maximum, VBM) of the photocatalyst should be above the proton reduction potential ($H_2/H^+ = 0$ V vs. NHE, pH = 0) and below the water oxidation potential ($H_2O/O_2 =$ 1.23 V, vs. NHE, pH = 0), respectively.

In addition to the thermodynamic requirements, there are also kinetic challenges in photocatalytic water splitting. The generation, separation and transfer of photogenerated carriers typically occur in the range of a few femtoseconds to nanoseconds; however, the surface redox reactions take much longer (microseconds to seconds), resulting in rapid recombination of photogenerated charge carriers.[4–6,27] To overcome this obstacle, sacrificial agents that react more readily with photogenerated carriers, are usually required. The H_2 production or O_2 evolution reactions with the assistance of sacrificial agents are referred to half-reactions, in which only the positions of LUMO/CBM and/or HOMO/VBM are required for redox reactions in thermodynamics. In addition, it should be noted that some sacrificial agents can also release H_2 by photoreforming.[28] Moreover, the overpotential, which means the potential difference above the equilibrium potential, should be overcome.[27a] Consequently, the introduction of suitable co-catalysts is preferred to reduce the overpotential.[4,6,29]

3.2. Photocatalytic Hydrogen production

The attempt to use MOFs for photocatalytic hydrogen production dates back to 2009.[30] In this work, a Ru-based MOF was adopted to provide the active sites for H_2 production in the presence of $Ru(bpy)_3Cl_2$, MV^{2+} (N,N′-dimethyl-4,4′-bipyridinium), and ethylenediaminetetraacetic acid disodium (EDTA-2Na). Since then, a diversity of MOF systems have been developed to split water into hydrogen under light irradiation.[31] In early-stage reports, MOFs were basically used as an alternative to conventional inorganic or molecular photocatalysts, where a dye-sensitization strategy,[32] the formation of heterojunctions,[33] the introduction of active species,[34] etc., were employed to improve their light-response and hydrogen production activity. With gradually deepening research, MOFs present their unique advantages in photocatalysis, especially in the exploration of structure-performance relationships.[9] In the following sections, we mainly discuss the modulation of photosensitive organic linkers and catalytic sites in MOFs to illustrate the structure-activity relationship in photocatalytic hydrogen production in the presence of sacrificial agents.

3.2.1. The Regulation of Photosensitive Organic Linkers

The organic linkers usually serve as antennas for light harvesting in MOF photocatalysis.[9] The photoresponse of MOFs was found to be adjustable via linker modification for enhanced photocatalytic performance since 2010.[28] UiO-66, a stable MOF was performed to split water into hydrogen under light irradiation. Though it did not display activity under visible light due to its negligible visible light response. To increase its photosensitivity, the 1,4-dicarboxybenzene (BDC) linker in UiO-66 was replaced with BDC-NH_2 to give isoreticular UiO-66-NH_2. The absorption spectrum was remarkably extended to the visible region by -NH_2 group decoration, leading to H_2 production activity under visible light irradiation. Light absorption is an important aspect of an excellent photocatalyst.[4–6] The diversity of linkers in MOFs enables flexible regulation of their light absorption. The π-electron rich linkers,[21a,d,31f,35] such as porphyrins, phthalocyanine, pyrene, etc., and modification of organic linkers with electron-rich groups,[19b,31c–e] such as -NH_2, -OH, -SH, etc., have been introduced to MOF skeletons to improve photosensitivity.

Not limited to light absorption, the linker distribution in MOFs was found to exert a unique influence on photocatalysis.[36] Two isoreticular single crystals of UiO-68 and its photoactive analog of UiO-68-TZDC were prepared by high-throughput synthetic methodologies. To elucidate the impact of the TZDC distribution on photocatalytic performance, UiO-68-$TZDC_x$ (x represents the TZDC ratio) was synthesized via a solvent-assisted linker exchange (SALE) process. With the increase of the TZDC precursor concentration, fluorescence confocal microscope indicated that TZDC gradually diffused from the periphery to the interior of UiO-68 and gradually formed a uniform distribution (Figure 3a). Interestingly, as the MOF structure changed from a core-shell to a homogeneous structure, the photocatalytic H_2 production activity exhibited a volcano-shaped curve and reached its maximum at x = 10 %. Furthermore, by prolonging the TZDC exchange time, the structure of UiO-68-$TZDC_{10\%}$ changed from a core-shell to a homogeneous structure and the photocatalytic activity decreased, further illustrating the higher activity of the core-shell structure (Figure 3b). This work highlights the influence of photosensitizer distribution on photocatalytic performance.

MOFs are constructed by metal nodes and organic linkers, where LMCT, LLCT, metal-to-linker charge transfer (MLCT) and metal-to-metal charge transfer (MMCT) processes can be involved in the charge transfer paths of MOFs. Thereby, modulation of linkers can easily regulate the charge separation efficiency of MOFs. Typically, the LMCT energies (E_{LMCT}) of UiO-66(Ce)-X with different functional groups were investigated by theoretical calculations.[19a] The density functional theory (DFT) calculation results indicated that there was a more negative E_{LMCT} in the MOFs with electron donating groups (such as -NH_2), which is more favorable for charge separation. Several experiments have confirmed this theoretical prediction. For example, the photocatalysts of x%-MIL-125-$(SCH_3)_2$ were prepared through an SALE process and photoelectrochemical characterizations manifested that the introduction of -SCH_3 promoted photogenerated charge separation and carrier density.[31e] Similarly, UiO-66 modified by BDC-$(SCH_3)_2$ and BDC-$(SOCH_3)_2$ was fabricated as a platform to investigate the effect of linkers on charge separation efficiency (Figure 4a).[37] Photoelectrochemical characterizations and femtosecond transient absorption spectroscopy revealed the enhanced charge separation efficiency in mixed-linker UiO-66. Most recently, Jiang and co-workers

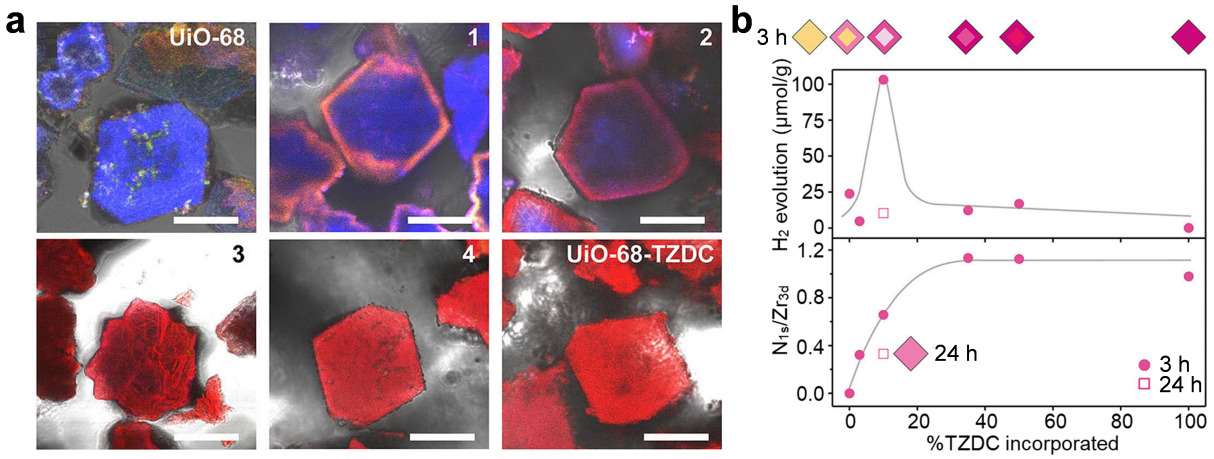

Figure 3. (a) Fluorescence confocal microscope images of UiO-68, UiO-68-TZDC$_x$ and UiO-68-TZDC, the scale bars correspond to 25 and 10 μm for UiO-68 counterparts and UiO-68-TZDC, respectively. (b) The amount of H_2 production after 6.5 h photocatalytic reaction of UiO-68, UiO-68-TZDC and UiO-68-TZDCx solids (x = 3, 10, 35, and 50%) prepared at 3 (filled circles) and 24 h (empty square). Adapted with permission.[36] Copyright 2021, American Chemical Society.

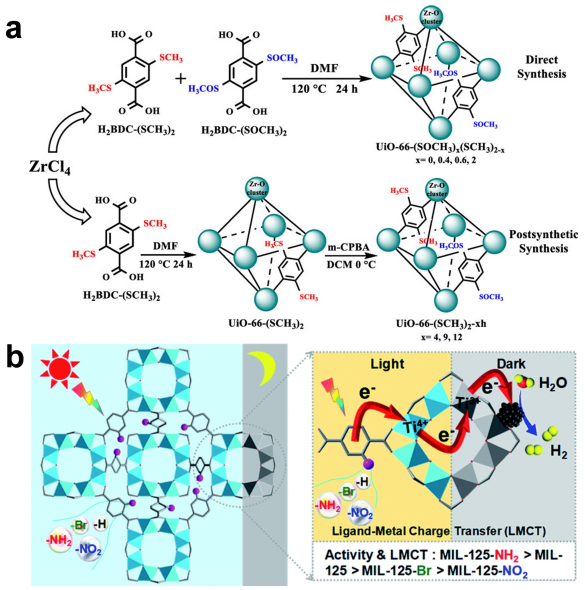

Figure 4. (a) The preparation of UiO-66 based on BDC-$(SCH_3)_2$ and BDC-$(SOCH_3)_2$ linkers. Reproduced with permission.[37] Copyright 2021, American Chemical Society. (b) Illustration showing MIL-125 and MIL-125-X (X = NH_2, NO_2, Br) for dark photocatalysis. Reproduced with permission.[38] Copyright 2022, The Royal Society of Chemistry.

found that MIL-125-X can mimic the natural dark reaction and demonstrated the significant linker substituent effects on charge separation and dark reaction activity (Figure 4b).[38] MIL-125 is constructed by the Ti-oxo cluster and BDC linker, featuring an evident photochromism under light irradiation due to the long-lived Ti^{3+} with electron storage capability. The color of MIL-125 changed shortly from white to blue and electrons were reserved in Ti-oxo clusters under light irradiation. When the Pt nanoparticles (NPs) were introduced as an electron acceptor into the photoexcited system, the electrons transferred immediately from the Ti-oxo cluster to the Pt cocatalyst to drive hydrogen production accompanied by gradual color fading in the dark. Significantly, UV/Vis absorption and in situ EPR spectra demonstrated the electron donating effect of the substituents can greatly prolong the Ti^{3+} lifetime and accelerate charge transfer, resulting in superior dark photocatalysis.

3.2.2. The Regulation of Catalytic Sites

The high overpotential is an important obstacle for photocatalytic H_2 production by using the pristine MOF. Therefore, suitable cocatalysts, particularly Pt NPs, are commonly incorporated into MOFs to reduce the overpotential of hydrogen production and promote charge separation. The size, distribution, and interfacial environment of Pt NPs exert remarkable impacts on charge separation and photocatalytic activity.[23a,34c,39] The Pt NPs with small size can promote charge transfer efficiency, and thus enhance photocatalytic H_2 production activity.[39b] However, the small size leads to agglomeration due to the high surface energy, which can possibly be suppressed by the confinement effect of MOFs. Typically, Wang et al. reported two stable and photoactive UiO-type MOFs loading Pt NPs for photocatalytic hydrogen production. The small Pt NPs of 2–3 nm and 5–6 nm were obtained in the MOFs with different pore sizes by in situ photo-deposition method (Figure 5a).[40] The resulting Pt@MOFs displayed good recyclability and high stability in photocatalytic reaction. Using a similar synthetic strategy, Pt NPs were introduced into the pores of Pd-PCN-222(Hf) by in situ solvent reduction approach, and the Pt NPs grew along the orientation of the pore with 3 nm width and 7–15 nm length (Figure 5b).[41] The composites displayed a high photocatalytic H_2 production rate of 22674 $\mu mol\,g^{-1}\,h^{-1}$. More importantly, the Pt NPs retained their original morphology and dispersion after the reaction. In fact, a lot of studies underline the excellent confinement

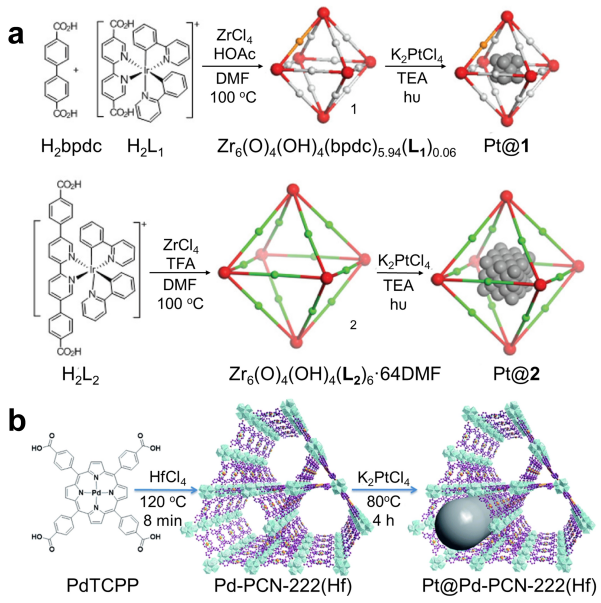

Figure 5. (a) The preparation of Pt@MOFs by in situ photo-deposition. Adapted with permission.[40] Copyright 2012, American Chemical Society. (b) Procedures of fabricating Pt@Pd-PCN-222(Hf). Adapted with permission.[41] Copyright 2019, The Royal Society of Chemistry.

effect of MOFs for the stabilization of active metal species.[23a]

Supporting surfactant-protected metal NPs as cocatalysts on supports is usual, where the morphology and size of metal NPs are more controllable. However, the role of the surfactant in photocatalysis remains unclear.[39a,42] To clarify this, Xu et al. investigated the influence of interfacial polyvinylpyrrolidone (PVP) between MOF and Pt cocatalyst on electron transfer in photocatalytic hydrogen production.[42b] The Pt NPs with different levels of PVP coverage were encapsulated into UiO-66-NH_2, in which Pt NPs and the MOF had similar morphology and size (Figure 6). Photocatalytic dynamic experiments suggested that the existence of PVP impeded interfacial charge transfer. As

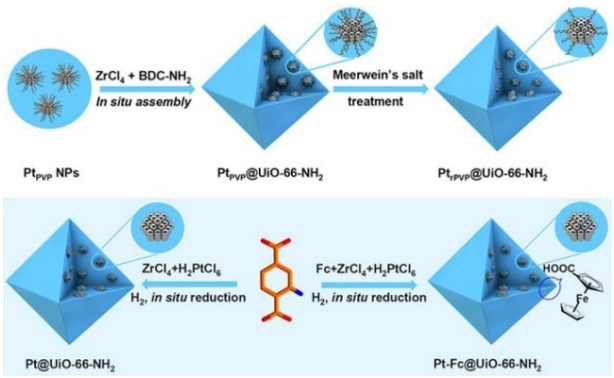

Figure 6. Schematic showing the synthetic strategies for introducing Pt NPs with different levels of PVP coverage and incorporating Fc electron mediator into UiO-66-NH_2. Adapted with permission.[42b] Copyright 2021, Wiley-VCH.

a result, the Pt@UiO-66-NH_2 with clean Pt surface presented the highest photocatalytic hydrogen production activity. To further accelerate the interfacial charge transfer, ferrocene carboxylic acid (Fc) was introduced as an electron mediator, leading to further enhanced photocatalytic activity. This work demonstrated the negative effect of surfactants on the surface of Pt cocatalyst in photocatalytic interfacial charge transfer and highlights the critical role of interfacial microenvironment for photocatalysis.

To date, the noble metal Pt is the most commonly used cocatalyst in photocatalytic hydrogen production. However, its high cost greatly limits its practical application. Therefore, it is necessary to minimize the noble metal loading and develop noble-metal-free cocatalysts. Single-atom catalysts have been developed to minimize the noble metal amount and maximize the usage efficiency.[8e,h,43] In addition to decreasing the amount of noble metals, diverse noble-metal-free sites, such as metal complexes,[44] sulfides,[45] and phosphides,[46] etc., have been developed as cocatalysts for photocatalytic hydrogen production. Hydrogenase is considered to be the most active natural water reduction catalyst consisting of Fe and other base metals.[5] Pullen et al. incorporated a [FeFe]-hydrogenase analogs of [FeFe]-(dcbdt)$(CO)_6$ into UiO-66 to replace noble metal cocatalysts for photocatalytic hydrogen production.[44a] The homogeneous photosensitizer of $[Ru(bpy)_3]Cl_2$ was introduced to improve the photocatalytic activity under visible light irradiation. To promote the charge transfer efficiency between photosensitized units and hydrogenase, the [FeFe]-hydrogenase analogs were immobilized into a porphyrin-based MOF, ZrPF,[44b] giving rise to high photocatalytic hydrogen production rate under visible light irradiation.

Metal phosphides are evidenced to replace noble metals in various catalytic reactions, which can catalyze reduction reactions or undergo transformation to new active oxygen-containing catalysts in oxidation reactions.[46] The Stylianou group combined Ni_2P NPs with MIL-125-NH_2 for photocatalytic hydrogen production.[46a] The optimal photocatalyst exhibited a H_2 evolution rate of 894 $\mu mol\,g^{-1}\,h^{-1}$ which is 3 times higher than that of Pt/MIL-125-NH_2. To elucidate the reasons why the catalytic performance of Ni_2P is superior to that of Pt, Jiang and co-workers pre-synthesized monodisperse Pt and Ni_2P NPs and introduced them into UiO-66-NH_2 for photocatalytic hydrogen production. Both cocatalysts featuring similar loading amounts and particle sizes were uniformly dispersed in UiO-66-NH_2.[46b] Electrochemical tests indicated that Pt was thermodynamically more favorable than Ni_2P, but Ni_2P was superior in kinetics supported by kinetic experiments and ultrafast spectroscopy.

In addition, many base metal-complex catalysts have been developed for water splitting to produce hydrogen. However, these molecular catalysts suffer from poor recyclability and photoresponse. Integration of photosensitive units and molecular-based catalysts into MOFs offers a feasible solution to solving the challenges.[34d,44f] Typically, Lin and co-workers designed a Zr_6-mPT MOF with UiO-69 topology containing phenanthroline.[44f] A cuprous photosensitizing unit (CuPS) and Fe catalytic sites were integrated into one skeleton at a close distance (≈1 nm) by the phenanthroline

linker and μ_3-OH of $Zr_6O_4(OH)_4$ cluster, respectively, affording FeX@Zr_6-Cu (Figure 7a). In photocatalytic experiments, the optimal FeBr@Zr_6-Cu showed 10 times and 27 times higher than the hydrogen production activity of the combination of Zr_6-Cu and $FeBr_2$ and a mixture of homogeneous CuPS and $FeBr_2$, respectively. Besides the introduction of external photosensitizers, using organic linkers as photosensitizers is an easier way to establish proximity between photosensitizers and catalytic sites. The Jiang group immobilized high-loading (>4 wt%) single-atom Ni sites onto the Zr_6-oxo cluster of UiO-66-NH_2 via a microwave-assisted method, yielding Ni_1-X/UiO-66-NH_2.[44g] The periodic and close arrangement between the linker antenna and Ni sites can reduce the electron transfer distance and facilitate charge separation. To unveil the effect of different microenvironments around Ni sites on photocatalytic performance, different Ni sites of Ni_1-S, Ni_1-O, and Ni_1-S_{ox} were fabricated (Figure 7b), among which the activity of Ni_1-S/UiO-66-NH_2 was the best. The results suggest that MOFs not only stabilize the active sites, but also inherit the facile modification of homogeneous catalysts, while creating a close distance between catalytic centers and photosensitizers to improve charge transfer efficiency.

Considering the diversity of MOF components, the active metals for proton reduction, such as Ni, Cu, Pb, etc., can be directly adopted to construct MOFs, allowing for photocatalytic hydrogen production without guest cocatalysts.[47] Tanaka and co-workers reported a Pb-MOF, KGF-1, which was composed of three-dimensionally extended sulfur SBUs.[47c] Theoretical calculations and time-resolved microwave conductivity suggested KGF-1 had a semiconductor-like electronic structure with a high pseudo-photoconductivity comparable to that of conductive MOFs. In the presence of Na_2EDTA sacrificial agent, the pristine KGF-1 exhibited a photocatalytic H_2 production rate of 25.5 $\mu mol\,g^{-1}\,h^{-1}$ without additional cocatalysts (Figure 8a). A stable MOF nanobelt denoted as Ni-TBAPy-NB was prepared through exfoliating its single crystal for photocatalytic hydrogen production.[47d] The organic linker of 1,3,6,8-tetrakis(p-benzoic acid)-pyrene (H_4TBAPy) linker acted as the photosensitizer. The [Ni_3O_{16}] cluster nodes possess a similar chemical composition to that of NiO_x, which is widely employed as a cocatalyst for proton reduction (Figure 8b). The photocatalytic experiments were conducted in an aqueous solution in the presence of ascorbic acid as the sacrificial agent. Strikingly, the optimal apparent quantum efficiency (AQE) of this nanobelt reached 8.0% under 420±10 nm light irradiation without additional cocatalysts. The remarkable photocatalytic performance was ascribed to the highly efficient LMCT process.

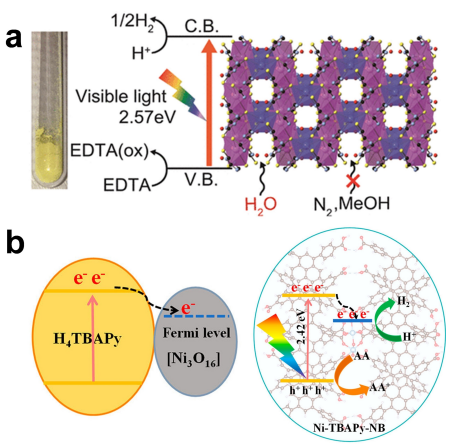

Figure 8. (a) Schematic illustration of the photocatalytic process of KGF-1. Reproduced with permission.[47c] Copyright 2020, American Chemical Society. (b) The photocatalytic hydrogen production mechanism of Ni-TBAPy-NB. Adapted with permission.[47d] Copyright 2022, American Chemical Society.

3.3. Photocatalytic Oxygen Production

In comparison with hydrogen production, the oxidation of water to O_2 is a four-electron process and involves several reactive intermediates, resulting in more challenging reaction kinetics.[6] In addition, the common sacrificial agents for water oxidation, such as $[S_2O_8]^{2-}$, Ce^{4+}, etc., have strong oxidizability.[4,5b] Accordingly, these impediments account

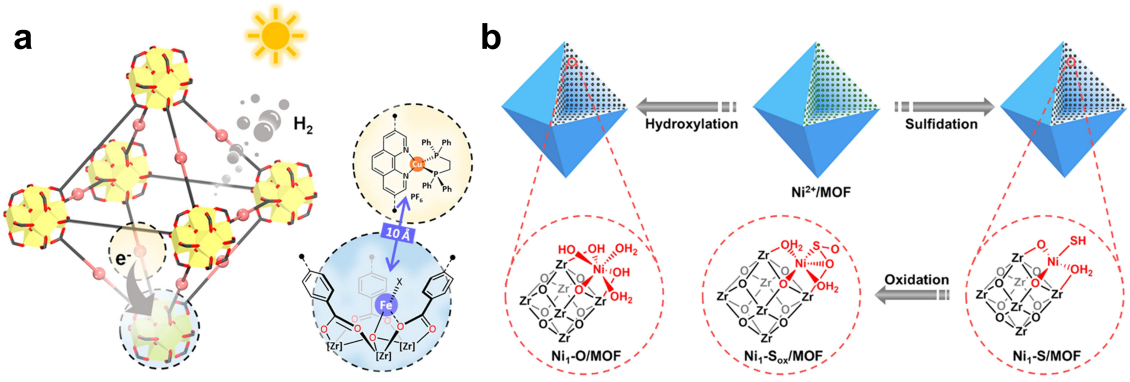

Figure 7. (a) The structure of the Cu photosensitizer and Fe catalytic sites in FeX@Zr_6-Cu. Adapted with permission.[44f] Copyright 2020, American Chemical Society. (b) Procedures of synthesis of Ni_1-X/UiO-66-NH_2 and their corresponding schematic structures. Adapted with permission.[44g] Copyright 2021, American Chemical Society.

for the very limited reports on photocatalytic water oxidation over MOFs.[31h,48]

Introducing catalytic sites capable of water oxidation is an effective strategy to achieve water oxidation in MOFs. Paille et al. incorporated $P_2W_{18}Co_4$ polyoxometalates (POM) into porphyrinic MOF-545 for photocatalytic oxygen production.[48a] The calculations indicated that $P_2W_{18}Co_4$ was located near two Zr_6-oxo clusters, where the interface between MOF and POM was connected via H-bonds, leading to a strong host-guest interaction to stabilize the POM (Figure 9a). Photocatalytic OER activity was performed in a borate buffer in the presence of $Na_2S_2O_8$ as the sacrificial agent. $P_2W_{18}Co_4$@MOF-545 presented the best OER activity among all counterparts, and the amount of O_2 evolution increased linearly and reached a plateau after 1 hour due to the exhaustion of $Na_2S_2O_8$ (Figure 9b). Subsequently, they processed the water oxidation system of $P_2W_{18}Co_4$@MOF-545 into a thin film device for electro- and photocatalysis (Figure 9c),[26b] which showed a higher turnover number (TON) than the above powder system.

Some stable Co- and Fe-based MOFs have been discovered to drive photocatalytic water oxidation due to the intrinsic water oxidation activity of Co-oxo and Fe-oxo clusters.[48c–f] In this case, the photosensitizer of $[Ru(bpy)_3]Cl_2$ was added to harvest visible light, while further efforts are needed to develop photocatalysts that can drive oxygen production under visible light irradiation. Previous work reported that Fe-UiO-66 achieved water oxidation and C–H activation by harvesting visible light,[21c] in which a metal-to-cluster charge transfer (MCCT) process occurred through modifying Fe^{3+} to the Zr-oxo cluster. These high-valent metals not only contribute to a narrow band gap to enhance light absorption, but are also beneficial to the stabilization of holes compared with organic linkers, facilitating the visible light-driven water oxidation.

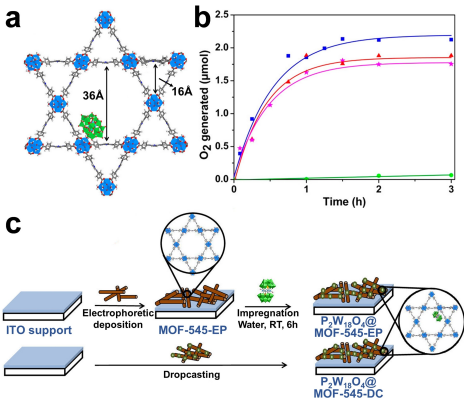

Figure 9. (a) The structure of $P_2W_{18}Co_4$@MOF-545, and (b) the kinetic plots of O_2 production of $P_2W_{18}Co_4$@MOF-545 (blue), $P_2W_{18}Co_4$@MOF-545 recycled once (red), twice (pink), and the mixture of homogeneous TCPP-H_2 and $P_2W_{18}Co_4$ in solution (green). Adapted with permission.[48a] Copyright 2018, American Chemical Society. (c) Schematic illustration of constructing $P_2W_{18}Co_4$@MOF-545 devices. Adapted with permission.[26b] Copyright 2019, American Chemical Society.

3.4. Photocatalytic Overall Water Splitting

Photocatalytic overall water splitting (OWS) is the process of dissociation of water to H_2 and O_2 without the addition of sacrificial agents, which is a grail reaction in photocatalysis.[4,6] There are very limited reports on photocatalytic OWS over MOFs, in which the activity remains rather low.[49]

Huang and co-workers reported the immobilization of the active hydrogen production site of Ni^{2+} into an Al-BDC-NH_2 MOF by coordination with -NH_2. In the photocatalytic process, the electrons produced by BDC-NH_2 were transferred to Ni^{2+} sites to participate in water reduction, while the holes reserved on the linker drove water oxidation.[49a] The dual-cocatalyst strategy was found to be effective for photocatalytic OWS over MOFs.[4,6d,29] Pt and RuO_x were introduced to MIL-125-NH_2, which successfully drive water splitting into H_2 and O_2.[49b] Furthermore, Zhang et al. achieved photocatalytic OWS by loading Pt and MnO_x inside and on the surface of UiO-66-NH_2, respectively (Figure 10).[49c] The spatially separated cocatalysts greatly accelerated the separation of electrons and holes and prolonged their lifetimes, promoting the OWS performance. Melillo et al. constructed a trimetallic UiO-66(Zr/Ce/Ti) for photocatalytic OWS, in which mixed metal UiO-66 was more favorable to water oxidation process than UiO-66, leading to a better OWS performance.[49d] Recently, a stable Ti-based MOF, IEF-11, was reported for photocatalytic OWS.[49e] Surprisingly, IEF-11 can drive photocatalytic OWS without activity loss over 10 days.

Single-component catalysts directly driving photocatalytic OWS remain a grand challenge because the bands must simultaneously satisfy the positions of H_2 and O_2 production. The Z-scheme is a two-step water splitting approach consisting of two different semiconductors that drive oxidation and reduction reactions, respectively, which can overcome the thermodynamic limitation of single-component photocatalysts.[4,6c] Recently, the Wang group assembled two MOFs for H_2 production and water oxidation reaction (WOR) into one liposome constructing a Z-scheme for photocatalytic OWS.[49f] The MOF for H_2 production was a Hf-based MOF nanosheet containing Zn-porphyrin as photosensitizers and Pt-porphyrin as water reduction sites, which was functionalized with pentafluoropropionic acid to create a hydrophobic surface. The WOR-MOF with hydrophilicity was constructed from Zr-oxo clusters and 2,2′-bipyridine-5,5′-dicarboxylic acid (BPYDC)

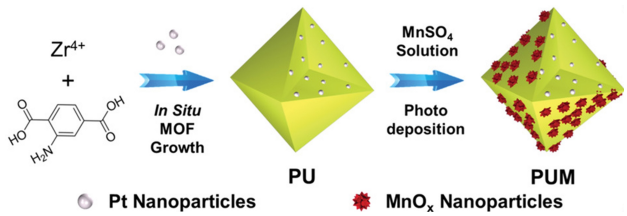

Figure 10. The synthetic route to Pt@UiO-66-NH_2@MnO_x. Adapted with permission.[49c] Copyright 2020, Wiley-VCH.

linkers, where the [Ru] and [Ir] molecular catalysts were incorporated by the BPYDC acting as photosensitizers and catalytic sites, respectively (Figure 11a and 11b). Both MOFs were installed in the hydrophobic bilayers and the aqueous phase of one liposome, respectively (Figure 11c). The carrier transport between the two MOFs was connected by the Fe^{3+}/Fe^{2+} and TCBQ/TCBQH redox relays to avoid charge recombination. The optimal hybrid system achieved photocatalytic OWS with an apparent quantum yield of (1.5 ± 1) %.

4. Photocatalytic CO_2 Reduction

The basic principle of photocatalytic CO_2 reduction is similar to that of water splitting. However, the CO_2 reduction process involves multiple proton-coupled electron transfer (PCET) processes accompanied by various intermediates on catalytic sites, leading to the challenge of regulating product selectivity.[3,5] In addition, CO_2 is a gas molecule bearing a large bond energy, and interacts weakly with a majority of catalysts, resulting in limited interactions. As a class of porous materials, MOFs are considered promising candidates for CO_2 capture.[7d,50] Furthermore, the structural tailorability of MOFs allows the installation of different active sites, which facilitates the regulation of various reaction intermediates for high selectivity. In this section, the photo-driven half reactions of CO_2 reduction involved in two-electron and multi-electron processes are first discussed. Next, given the structural compatibility of MOFs, the tandem reactions of 2-electron products to valuable products are introduced. In addition, the potential advantages of MOFs in the photoreduction of low CO_2 concentration are illustrated with examples. Finally, an overview of recent advances in the photocatalytic overall reaction of CO_2 is presented.

4.1. Half Reactions

4.1.1. Two-electron Process

Various metal complexes have been reported for the photoreduction of CO_2 to CO or HCOOH with high selectivity, but they usually suffer from deactivation and sluggish charge transfer during the reaction.[51] MOFs have been extensively applied as a platform to simultaneously integrate homogeneous photosensitizers and catalytic units for CO_2 photoreduction, which can address related challenges in molecular systems.[52]

In the early work reported by Lin and co-workers, a molecular photocatalyst, $Re^{I}(CO)_3(bpy)X$, was incorporated into the UiO-67 skeleton for photocatalytic CO_2 reduction. Under UV irradiation, the Re sites drive the reduction of CO_2 to CO, exhibiting higher stability than the homogeneous counterpart.[52a] To improve photocatalytic performance under visible light irradiation, the molecular photosensitizer of $[Ru(dmb)_3]^{2+}$ was physically mixed with a similarly structured MOF to drive CO_2 reduction under visible light irradiation.[52b] However, these photosensitizers are usually expensive and must be excessively introduced, and cannot be recycled after the reaction. Moreover, the random distribution of photosensitizers and MOFs in the reaction system is also not conducive to charge transfer. Integration of these photosensitive molecules with catalytic units into one MOF backbone has been developed to overcome the above drawbacks.[52c–g] Typically, the Cu photosensitizer and $Re(CO)_3Cl$ sites were incorporated into a single MOF to afford mPT-Cu/Re (Figure 12a).[52d] This composite drove photoreduction of CO_2 to CO with a 95-fold improvement over their homogeneous counterpart due to the close proximity between photosensitizers and Re sites accompanied by a faster charge transfer. Mahmoud et al. assembled a dicarboxylic acid linker containing photoactive $Ru(cptpy)_2$ sites with ZrO_8 clusters, resulting in a stable MOF named AUBM-4 (Figure 12b).[21b] In photocatalytic CO_2 reduction, an intramolecular MLCT process in which the electrons transferred from Ru to cptpy linker drove the photoreduction of CO_2 to HCOOH under visible light irradiation (Figure 12c). Recently, Liao and co-

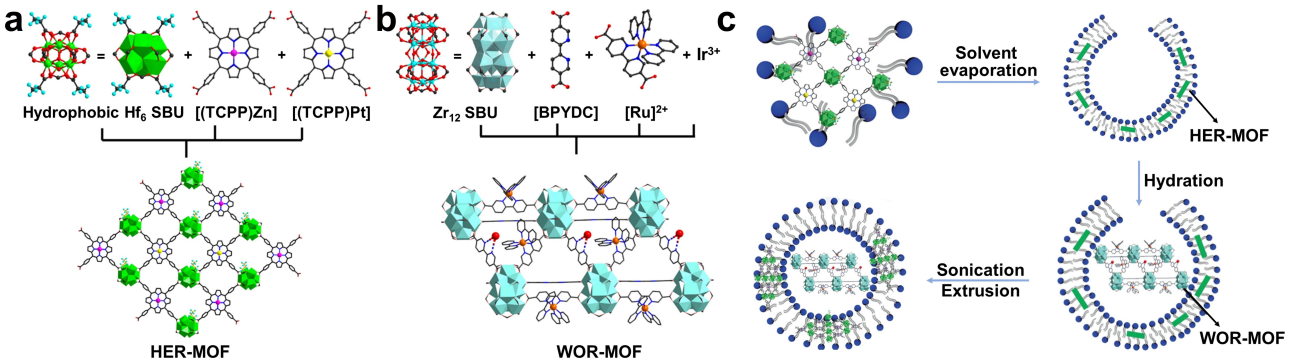

Figure 11. The structures of (a) MOF for H_2 production and (b) WOR-MOF. (c) Schematic illustration of assembling the two MOFs into liposome to construct Z-scheme. Adapted with permission.[49f] Copyright 2021, Nature Publishing Group.

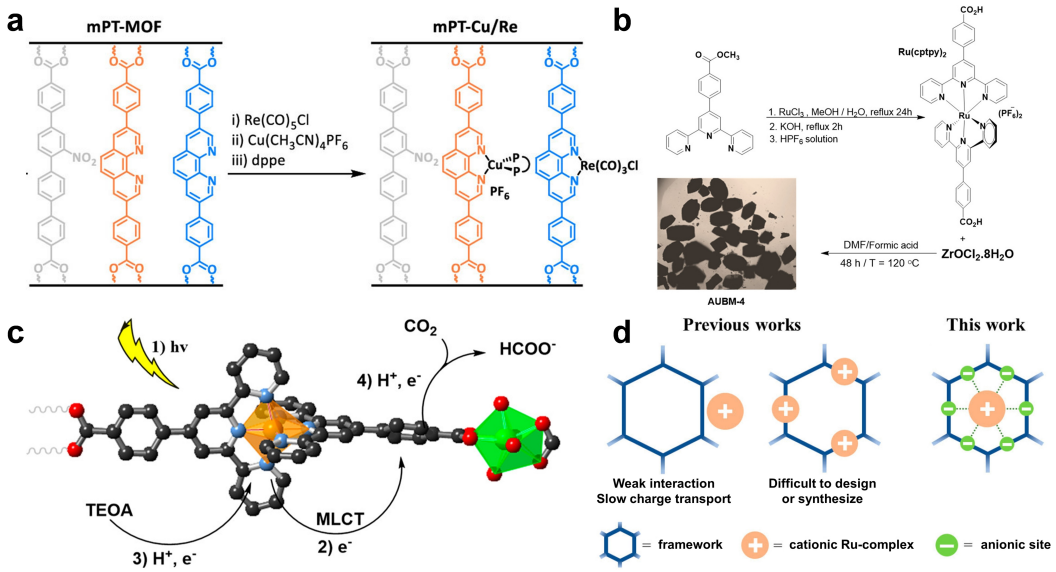

Figure 12. (a) Schematic diagram of integrating Cu photosensitizers and $Re(CO)_3Cl$ sites into a single MOF skeleton. Adapted with permission.[52d] Copyright 2020, American Chemical Society. (b) The procedure of synthesizing AUBM-4. (c) The proposed MLCT mechanism for CO_2 photoreduction over AUBM-4. Adapted with permission.[21b] Copyright 2019, American Chemical Society. (d) Schematic diagram of the electrostatic self-assembly strategy and its advantage over previous works. Adapted with permission.[52g] Copyright 2021, American Chemical Society.

workers developed an electrostatic self-assembly strategy, in which the electrostatic interaction between MOF and photosensitizer greatly stabilized the molecular photosensitizer and saved its amount.[52g] The negatively charged 2D framework of Cu-HHTP possessed a pore size of 1.66 nm, where the photosensitizer $[Ru(phen)_3]^{2+}$ was assembled into the pores of Cu-THPP via electrostatic interaction (Figure 12d). The strong interaction between the MOF and photosensitizers can greatly accelerate the charge transfer from $[Ru(phen)_3]^{2+}$ to Cu catalytic sites. As a result, although the amount of the photosensitizer was only approximately 1/500 compared with that in previous literature, the composite showed a high CO production rate of 130 mmol g^{-1} h^{-1} and even maintained high activity under natural sunlight.

The nature of MOFs greatly facilitates the structural regulation of both photosensitizers and active units for unveiling intrinsic mechanisms in photocatalytic CO_2 conversion. Zhuo et al. integrated $Ru(bpy)_3$ photosensitizer and Cu catalytic center into the Eu-bpy MOF for photocatalytic CO_2 reduction (Figure 13a).[52e] Interestingly, changing the coordination anion of Cu from Cl- or adenine to pyridine resulted in a decrease in the production of HCOOH, while the amount of CO increased greatly. Theoretical calculations revealed that the selectivity of CO_2 reduction was controlled by H-bond between the Cu sites and CO_2 intermediates, which was favorable for the intermediate hydrogenation to HCOOH instead of CO (Figure 13b). Pyridine suppressed H-bond formation, resulting in a lower energy barrier for CO formation. This work proposed an approach to control the selectivity of CO_2 photoreduction at molecular-level. In addition, the host-guest interaction between molecular photosensitizers and catalytic sites has a significant impact on photocatalytic

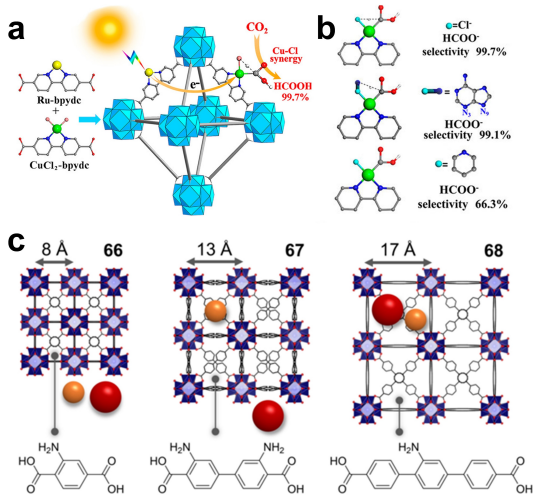

Figure 13. (a) Schematic diagram of integrating the Ru photosensitizer and the Cu catalytic unit into an Eu-bpy MOF for photocatalytic CO_2 reduction. (b) The H-bond interaction of different coordination anions with CO_2 and the corresponding photocatalytic selectivity to $HCOO^-$. Adapted with permission.[52e] Copyright 2021, American Chemical Society. (c) Schematic diagram of the different positions of the [Re] active site (orange) and the [Ru] photosensitizer (red) in UiO-66, -67, and -68. Adapted with permission.[52f] Copyright 2020, Wiley-VCH.

performance. To investigate these effects, Fischer, Warnan and co-workers immobilized the guests of molecular [Re] catalytic site and [Ru] photosensitizer into the hosts of isoreticular MOFs, i.e. UiO-66, -67, and -68, investigating the influence of different host-guest interactions on catalyst stability and charge transfer between the active center and photosensitizer in photocatalytic CO_2 reduction.[52f] Because of the different cavity sizes of isoreticular UiOs, the

[Re] and [Ru] complexes were anchored onto the particle surfaces of UiO-66; the [Re] and [Ru] were stabilized in the cavities and onto the surface of UiO-67, respectively; while both [Re] and [Ru] were inside the cavities of UiO-68 (Figure 13c). As a result, these composites presented very different photocatalytic activity and stability, highlighting the perfect candidate of MOFs as a platform to study the host-guest interactions of molecular-based catalysts.

The abundant modifiable sites in linkers and metal clusters, as well as the pore space enable the fabrication of MOF composites with diverse functional species for improved photocatalytic CO_2 conversion.[53] Ye and co-workers incorporated Co sites into the porphyrin units of MOF-525 for photocatalytic CO_2 reduction.[43d] The atomic dispersion of Co sites significantly accelerated charge separation, and promoted CO_2 activation. This work highlights the structural advantages of MOFs for stabilizing atomically dispersed active sites. Yaghi, Yang and co-workers prepared Ag nanocube@Re-MOF photocatalysts for CO_2 photoreduction (Figure 14a),[53a] where the Ag nanocube with a strong localized surface plasmon resonance (LSPR) effect can extend the photoresponse and lead to a strong electromagnetic field to promote the CO_2 reduction activity. TiO_2 is the most classic semiconductor for photocatalysis. Ultra-small anatase TiO_2 NPs were encapsulated into MIL-101 pores to form a heterojunction for CO_2 photoreduction (Figure 14b).[53d] The optimal composite exhibited an AQE of 11.3 % for the overall reaction of CO_2 to CO. Zhang and co-workers developed a template strategy to graft ultrathin Co-based and Cd-based MOLs on graphene oxide (GO) for photocatalytic CO_2 reduction.[53e] GO can not only stabilize the MOLs, but also act as an electron mediator to accelerate charge transfer, and the optimal Co counterpart showed an ultrahigh CO activity of 216.2 mmol g^{-1} h^{-1}. The integration of enzyme and MOF into one system to construct a semi-artificial photocatalyst is a promising avenue for high CO_2 photoreduction.[53f] Formate dehydrogenase was immobilized into photoactive NU-1006 for photocatalytic CO_2 reduction, where the Rh complex acted as an electron mediator to accelerate charge transfer between the enzyme and MOF. In the presence of the coenzyme NADH, the semi-artificial photocatalyst can selectively convert CO_2 to HCOOH with a high activity.

The CO_2 photoreduction activity of pristine MOFs was reported by the Li group at the very early stage.[54] The high-density Ti sites in MIL-125-NH_2 can drive CO_2 to HCOOH under visible light irradiation. To further extend the light response, a porphyrin MOF, PCN-222, was adopted for CO_2 photoreduction,[55] where HCOOH can be produced on the Zr-oxo clusters via the classical LMCT process. More importantly, a long-lived electron trap state in PCN-222 was detected by ultrafast transient absorption spectroscopy. This work highlights the advantages of the well-organized molecular arrangement in MOFs over random molecular systems.[55] Currently, both organic linkers and metal nodes of MOFs have been widely accepted as catalytic sites for photocatalytic CO_2 reduction.[56] In particular, the different facets of MOFs, which generally expose different ratios of linkers and metals in MOFs, can strongly affect photocatalytic performances.[57] Yang et al. fabricated two MOLs of Ni-MOL-100 and Ni-MOL-010 that exposed (100) and (010) facets, respectively, displaying different CO_2 photoreduction performance (Figure 15a).[57a] In comparison with the (010) facet, there were more coordination unsaturated Ni^{2+} sites with a close distance on the (100) facet. DFT calculations revealed that neighboring Ni sites interacted more strongly with CO_2, leading to bent absorption modes of CO_2 on the (100) facet. Consequently, Ni-MOL-100 exhibited better CO_2 photoreduction activity (Figure 15b). Likewise, Sun, Wang and co-workers developed an ultrasound-assisted method to fabricate ultrathin MIL-125-NH_2 nanosheet with exposed (110) facet, denoted T110NS.[57b] T110NS exhibited higher CO_2 reduction activity than bulk NH_2-MIL-125 exposed to (001), (110), or (111) facets. DFT calculations and kinetic characterizations manifested the superior performance of T110NS resulting from the exposed abundant Ti atoms that are beneficial to charge separation.

4.1.2. Multi-electron Process

The multi-electron reduction of CO_2 to hydrocarbons, alcohols and C_{2+} products is more attractive yet more

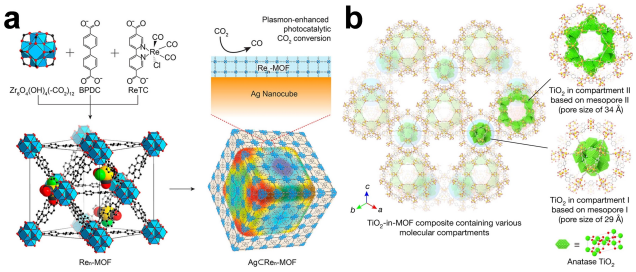

Figure 14. (a) The structures of Re-MOF and the schematic diagram of plasmon-enhanced photocatalytic CO_2 reduction over Ag nanocube@Re-MOF. Adapted with permission.[53a] Copyright 2017, American Chemical Society. (b) Schematic diagram of the TiO_2-in-MOF composites. Reproduced with permission.[53d] Copyright 2020, Nature Publishing Group.

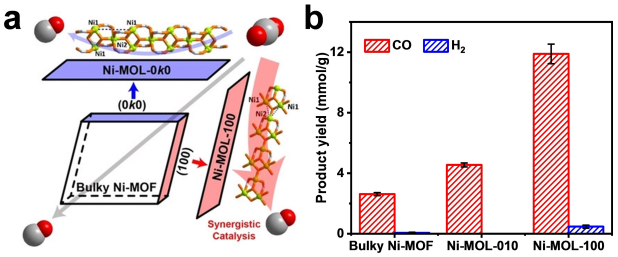

Figure 15. (a) Schematic diagram of bulky Ni-MOF, Ni-MOL-010, and Ni-MOL-100 and their different environments of Ni sites. (b) The CO_2 photoreduction over Ni-MOF, Ni-MOL-010, and Ni-MOL-100. Adapted with permission.[57a] Copyright 2021, Wiley-VCH.

challenging than the above two-electron reduction process to CO and/or HCOOH.[6c,58] Although the energy required in thermodynamics decreases with the increasing number of electrons involved in the CO_2 photoreduction (Figure 1), the process involves multi-step hydrogenation and/or C–C coupling processes accompanied by diverse intermediates, giving rise to significant challenges in product selectivity.[58] MOFs feature highly designable structures for rationally configuring various active sites to modulate the interaction with different intermediates in photocatalytic CO_2 reduction, thereby possibly promoting the selectivity of multi-electron products.[59]

Particularly, the formation of CH_4 is an 8-electron process that requires the highest electron number among the C_1 products of CO_2 reduction. Inspired by dynamic active sites in enzymatic catalysis, a self-adaptive dual-metal-site pairs (DMSPs) was developed to spontaneously modulate the ad-/de-sorption of the diverse intermediates in the photoreduction of CO_2 to CH_4, achieving a high photocatalytic CH_4 selectivity.[59b] The self-adaptive DMSPs were fabricated by means of modifying the flexible ethylenediaminetetraacetic acid (EDTA) chelating Cu and Ni sites onto the coordinatively unsaturated Zr-oxo clusters of MOF-808 (Figure 16a). Theoretical calculations revealed the dynamic behavior of the DMSPs (Figure 16b) and the continuously evolving arrangement of dual sites keep the optimal bonding energy with different C1 intermediates, thus preventing the desorption of intermediates into by-products. The interfacial H-bond stabilizes these intermediates to finally produce CH_4.[59f] The Ng group incorporated Cu_2O nanowires into $Cu_3(BTC)_2$, affording core-shell composites of $Cu_2O@Cu_3(BTC)_2$. The hybrid catalyst gave rise to a 100 % selectivity for photocatalytic CO_2 reduction to CH_4. The infrared spectra revealed the existence of rich uncoordinated carboxyl groups at the interface between Cu_2O and the MOF, which can form hydrogen bonds with the *CO, *CHO, *CH_2O, and *OCH_3 reduction intermediates of CO_2. The hydrogen bond interaction can stabilize these intermediates to prevent their desorption, resulting in a lower energy barrier for CH_4 production.

In comparison with the conversion of CO_2 to multi-electron C_1 products, there are very few examples on the extra C–C coupling process to C_{2+} products by MOF photocatalysis.[59c,d] The Cu-based catalysts have shown superior performance for C–C coupling to C_{2+} products.[60] Wang et al. reported a photoinduction method (PIM) to anchor Cu single atoms (Cu SAs) on UiO-66-NH_2 (Figure 17a), where calculations revealed that Cu SAs facilitated the formation of CHO* and CO* intermediates that are readily coupled on Cu sites to CH_3CH_2OH, achieving a higher photoreduction activity of CO_2 to CH_3OH and CH_3CH_2OH than that of Cu NPs/UiO-66-NH_2 and the parent MOF (Figure 17b).[59c] Except for classical Cu sites, the construction of a Zr-O-Mo interface has also been reported to assist C–C coupling.[59d] The authors pre-synthesized the missing-linker defective UiO-66, followed by reacting with MoS_2 precursor resulting in the hybrid material of d-UiO-66/MoS_2. The Zr-O-Mo interface can reduce the energy barrier of HOOC-COOH* formation and accelerate multi-step hydrogenation process, thereby promoting the CH_3COOH production (Figure 17c). As a result, the optimal hybrid photocatalyst showed a photocatalytic CH_3COOH production activity of 39.0 $\mu mol\,g^{-1}\,h^{-1}$ with H_2O vapor as the electron donor (Figure 17d).

4.1.3. Tandem Reaction

Compared with inert CO_2, CO is a more active feedstock, which has been extensively employed to prepare C_{2+} products and fine chemicals such as alcohols, aldehydes and carboxylic acids.[61] However, the colorless, odorless, and toxic CO gas is dangerous in both laboratorial and industrial applications. Given the recent advances in the photoreduction of CO_2 to CO with high activity and selectivity, the conversion of CO from photocatalytic CO_2 reduction into valuable products through tandem reactions would be promising.[61a] In tandem reactions, the cooperative involvement of multiple catalytic sites is required,

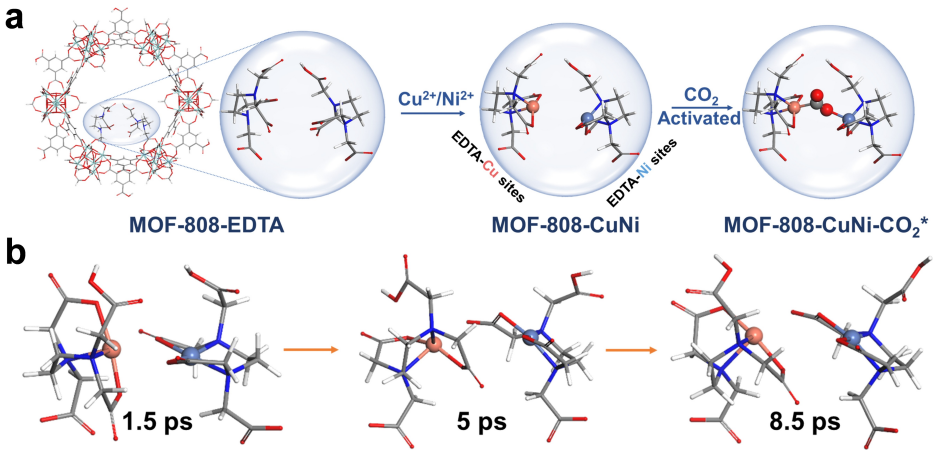

Figure 16. (a) Illustration of the structure of MOF-808-CuNi. (b) The dynamic behavior of dual-metal sites. Adapted with permission.[59b] Copyright 2021, Nature Publishing Group.

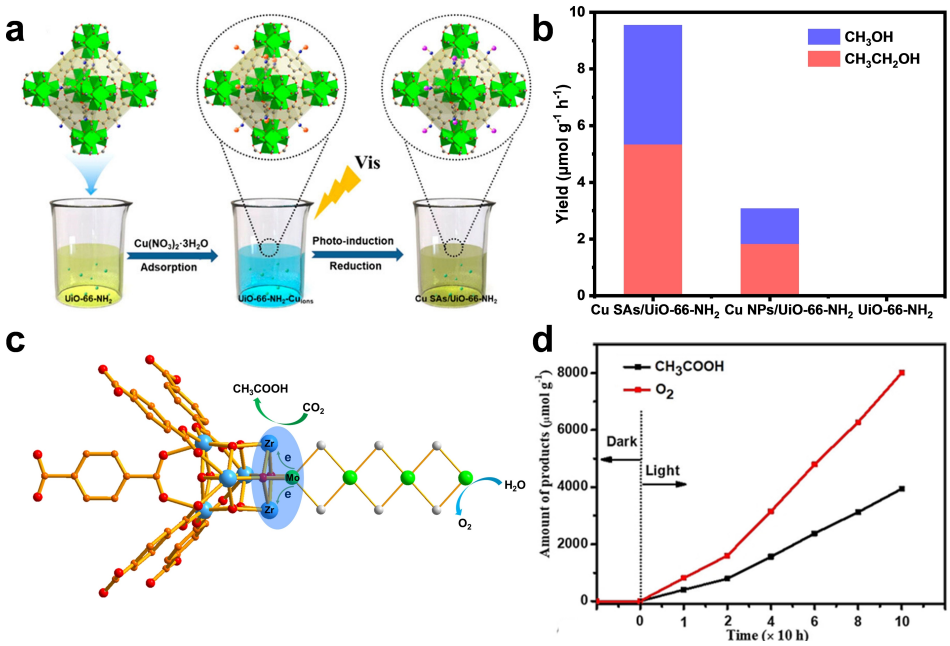

Figure 17. (a) Synthetic scheme for the synthesis of Cu SAs/UiO-66-NH_2 photocatalyst. (b) The photocatalytic CO_2 reduction performance of different counterparts. Adapted with permission.[59c] Copyright 2020, American Chemical Society. (c) Schematic diagram of the Zr-O-Mo interface promoting photoreduction of CO_2 to CH_3COOH over d-UiO-66/MoS_2. (d) Kinetic plot of photocatalytic CO_2 reduction over d-UiO-66/MoS_2. Adapted with permission.[59d] Copyright 2021, Wiley-VCH.

thereby MOFs would be a good candidate for easily integrating various active sites into a single framework.[62]

Ni-based MOFs usually exhibit high selectivity in the photoreduction of CO_2 to CO, which is favorable for subsequent conversion.[9c,f] Niu et al. reported a spongy Ni-based MOF for photocatalytic CO_2 reduction, which presented high activity and near 100 % selectivity in the photoreduction of CO_2 to CO. Subsequently, Ag NPs were decorated on the surface of the Ni-MOF, and the CO was further converted into CH_3COOH with high activity (Figure 18a).[62a] Carbonyl synthesis is an important industrial reaction by using CO as feedstock. Zhang and co-workers integrated ultrafine CuPd NPs into PCN-222(Co) to drive photocatalytic carbonylation reactions through a tandem reaction, in which the toxic CO was replaced with CO_2 as the starting material.[62b] In this tandem reaction, PCN-222(Co) initially reduced CO_2 to CO with a high selectivity, meanwhile, the incorporated CuPd NPs can catalyze a Suzuki coupling reaction of iodobenzene and phenylboronic acid, in which CO inserted into the phenyl-Pd-I intermediate to yield the final benzophenone (Figure 18b). The tandem reaction mechanisms were proposed based on ^{13}C-labeled and control experimental results. Recently, the Lan group reported that a bulk MOF, NNU-55-Ni, could be in situ spontaneously exfoliated into nanosheets during photocatalytic CO_2 reduction to CO. The produced CO was transferred into a chamber reactor to synthesize a series of diethyltoluamides by participating in the aminocarbonylation reaction in the presence of $Pd(PPh_3)_4$ as the catalyst.[62c]

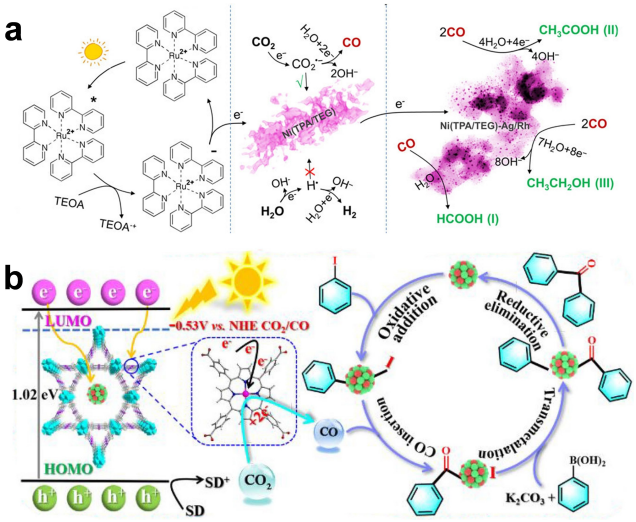

Figure 18. (a) Schematic diagram of the tandem reaction for converting CO_2 to CH_3COOH. Reproduced with permission.[62a] Copyright 2017, The American Association for the Advancement of Science. (b) The tandem synthesis of benzophenone through CO_2 as feedstock. Reproduced with permission.[62b] Copyright 2021, American Chemical Society.

4.1.4. Low Concentration CO_2 Reduction

Currently, the reported works of CO_2 photoreduction are generally investigated in pure CO_2. However, the concentration of CO_2 available from actual industrial processes is low. In terms of high CO_2 enrichment capacity of MOFs, it is possible to achieve low pressure CO_2 photoreduction.[63]

The CO_2 enrichment capacity in MOF pores for low-pressure CO_2 photoreduction was confirmed by Kitagawa and co-workers.[63b] The molecular catalyst H_2RuCO was incorporated into UiO-67 by post-synthetic exchange (PSE) method, affording Zr-bpdc/RuCO composite. The composite exhibited a high affinity for CO_2. As a result, it maintained the high activity for photoreduction of CO_2 to HCOOH even under 5 % CO_2 (Figure 19a). Similarly, the TiO_2/UiO-66 composite showed potential for low-pressure CO_2 reduction even under 2 % CO_2.[63c]

Proton reduction is the major competitive reaction during photocatalytic CO_2 reduction; therefore, suppressing proton reduction is an essential solution to low pressure CO_2 reduction. Typically, a Ni-MOF monolayer (Ni MOL) displayed higher selectivity than Co MOL in the photoreduction of dilute CO_2 to CO.[63d] The stronger CO_2 but weaker H_2O adsorption energy of Ni MOL was responsible for its higher selectivity (Figure 19b). Zhang, Liao and co-workers constructed a series of isoreticular MOFs whose metal nodes were modified by Cl or OH.[63e] For low pressure CO_2 photoreduction, the nodes modified by OH presented a higher activity than those modified by Cl (Figure 19c). DFT calculations manifested that OH can significantly weaken the binding energy of H_2O with metal nodes while enhancing the CO_2 absorption (Figure 19d), resulting in the higher selectivity.

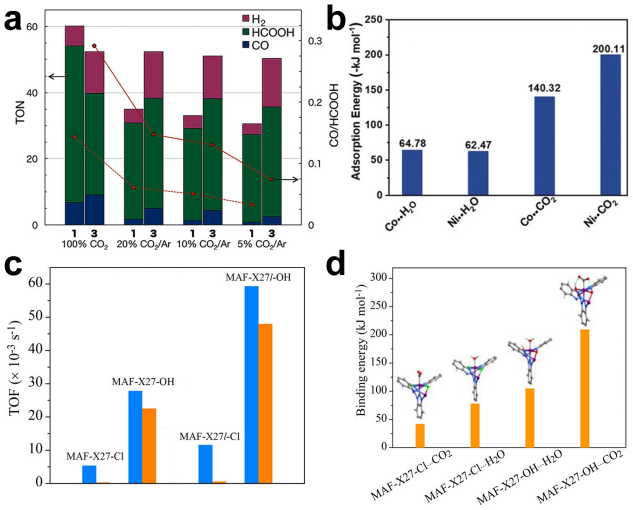

Figure 19. (a) The photocatalytic CO_2 reduction performance of Zr-bpdc/RuCO (**3**) and homogeneous $[Ru^{II}(bpy)(terpy)(CO)](PF_6)_2$ (**1**) under different CO_2 pressures. Adapted with permission.[63b] Copyright 2016, Wiley-VCH. (b) The CO_2 and H_2O adsorption energies of Ni MOLs and Co MOLs. Adapted with permission.[63d] Copyright 2018, Wiley-VCH. (c) The photocatalytic CO_2 reduction over MOFs modified by -Cl or -OH under pure CO_2 (blue) and 0.1 atm CO_2 (orange), and (d) the binding energies of OH and Cl counterparts with H_2O and CO_2. Adapted with permission.[63e] Copyright 2018, American Chemical Society.

4.2. Overall Reaction

The overall photocatalytic CO_2 reduction means that photocatalysts drive CO_2 reduction with H_2O directly in the absence of sacrificial agents. In contrast to the very few examples in photocatalytic OWS, the overall reaction of CO_2 photoreduction with water vapor under gas-solid mode has been reported with more examples.[64] The overpotential for water vapor oxidation is lower than that of aqueous water, which may account for a relatively easier overall CO_2 photoreduction process in the gas-solid mode. In addition, the products of the gas-solid mode are prone to hydrocarbons due to the easier deoxygenation process of CO_2.[65] Some classical MOFs have achieved photocatalytic overall CO_2 reduction in gas-solid mode.[59d,e,66] The Cao group systematically investigated the influences of the strong coordination interaction between linkers and metal nodes on photocatalytic CO_2 reduction under gas-solid condition.[59e] The investigated PCN-601 consisted of Ni-oxo cluster coordinated with porphyrin via pyrazolyl groups (Figure 20a), with a stronger bond strength than the analogous PCN-222 formed by carboxylate porphyrin linker. The DFT calculations and kinetic experiments suggested that the strong interaction between the pyrazolyl group and Ni-oxo cluster significantly accelerated the LMCT process. As a result, PCN-601 achieved a photocatalytic overall CO_2 reduction with CH_4 and H_2O_2 as products, the activity of which was far superior to that of PCN-222, homogeneous Ni_3TCPP and Pt/CdS (Figure 20b). This work highlighted the importance of coordination spheres on MOF photocatalysts. Similarly, the mixed-metal porphyrinic Ti/Zr-MOF-525 showed higher selectivity and activity in the photoreduction of CO_2 to CH_4 than their single-metal counterparts.[66b]

Despite the great progress in gas-solid phase overall CO_2 photoreduction, this overall reaction in liquid phase indeed remains a great challenge.[67] Recently, the integration of CO_2 reduction and H_2O oxidation catalysts into a single framework has shown the progress.[67b,c] The Ru-bipyridyl complexes and Co-imidazolate sites are classic water oxidation and CO_2 reduction sites in photocatalysis, respectively. Huang et al. incorporated $[Ru(Hip)_3]Cl_2$ into MAF-34-Co to partially replace cobalt sites, yielding MAF-34-CoRu (Figure 21a).[67b] The $[Ru(Hip)_3]Cl_2$ unit acted as both a photosensitizer and an oxygen production site. In

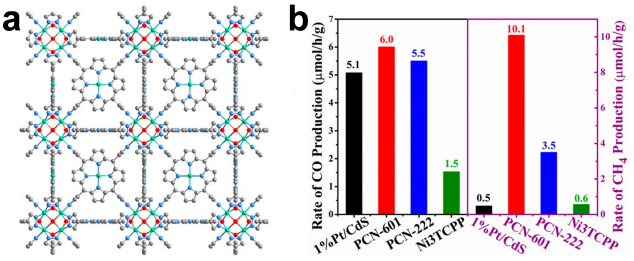

Figure 20. (a) The structure of PCN-601. (b) The photocatalytic CO_2 reduction activity of different photocatalysts. Adapted with permission.[59e] Copyright 2020, American Chemical Society.

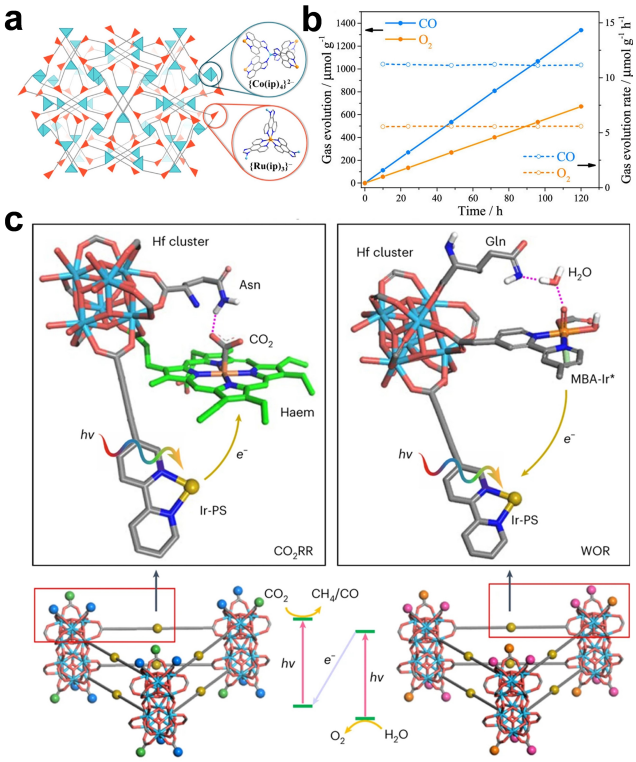

Figure 21. (a) The topology structures of MAF-34-CoRu and (b) its photocatalytic CO_2 reduction plots along with time. Reproduced with permission.[67b] Copyright 2022, American Chemical Society. (c) Schematic diagram of photocatalytic overall CO_2 reduction over the Z-scheme formed by (left) CO_2 reduction and (right) water oxidation MOZs. Adapted with permission.[67d] Copyright 2022, Nature Publishing Group.

the absence of any sacrificial agent, MAF-34-CoRu achieved the photocatalytic overall CO_2 reduction with 100 % selectivity of CO accompanied by stoichiometric O_2 (Figure 21b). Subsequently, MAF-34-CoRu was adopted to drive CO_2 photoreduction in 15 % diluted CO_2 reduction under the gas-solid mode which maintained a comparable performance to pure CO_2. In another work, the heterometallic Fe_2M cluster in NNU-31-M was applied to drive overall CO_2 photoreduction,[67c] where the high valent Fe and low valent metal M (M = Zn, Co, Ni) were proposed to participate in H_2O oxidation and CO_2 reduction, respectively. The optimal NNU-31-Zn exhibited the highest HCOOH yield with 100 % selectivity and stoichiometric O_2. Inspired by natural photosynthesis, the fabrication of Z-scheme has been developed to drive overall CO_2 photoreduction. Recently, Lan et al. developed MOF-based artificial enzymes (MOZ) for CO_2 photoreduction, where catalytic sites, photosensitizers, and amino acids (AA) were integrated into one MOF monolayer.[67d] The AAs with small pK_a in MOZ can accelerate the PCET process, and the AAs with high pK_a will provide H-bond interactions with CO_2 and related intermediates, accordingly promoting CO_2 reduction. The optimal artificial enzyme showed high TON and selectivity in CO_2 photoreduction. Meanwhile, photocatalytic WOR can also be achieved by altering the composition of MOZ. As a result, the MOZs respectively bearing the capabilities of WOR and CO_2 reduction were integrated into one system to construct a Z-scheme, achieving the overall CO_2 photoreduction (Figure 21c).

5. Advanced Characterization Techniques

In efforts to design highly efficient photocatalysts, characterization techniques are crucial to unveil the light absorption, charge separation, and surface redox reactions in photocatalysis. The characterization techniques for photocatalysis have been mentioned in several reviews.[68] Given that the atomically well-defined and tailorable structures of MOFs offer a great opportunity to explicitly understand photocatalytic mechanisms, advanced techniques appear to be particularly important. In this section, we first focus on time- and space-resolved techniques to disclose charge reaction kinetics in MOF photocatalysis. Then diffuse reflectance infrared Fourier transform spectroscopy, electron paramagnetic resonance spectroscopy, and X-ray photoelectron spectroscopy for identifying photocatalytic intermediates and related mechanisms are discussed.

5.1. Transient Absorption Spectroscopy

Electrochemical measurements, such as electrochemical impedance spectroscopy (EIS), transient photocurrent, fluorescence emission, etc., provide convenient access to disclose the charge transfer kinetics. However, the time-resolution of electrochemical techniques is only in the level of microseconds to seconds.[68a] Transient absorption spectroscopy (TAS) is a pump-probe technique, in which the photocatalysts are excited by pump light followed by monitoring of the relaxation process via the probe light.[68c] Depending on the frequency of the pulsed laser, the time-resolution of TAS is in the range from fs to ns. Recently, fs-scale ultrafast TAS has become a powerful tool to reveal the photocatalytic charge transfer behaviors in MOFs.[17,33b,43a,49f]

The modification of organic linkers in MOFs with electron-rich groups, such as -NH_2, is a common approach to extend light absorption. The charge separation kinetics of two representative photoactive MOFs, MIL-125 and MIL-125-NH_2, were studied by ultrafast TAS in combination with visible light and mid-IR probes, revealing that the -NH_2 can not only promote the light response but also stabilize the holes to prolong charge lifetime as well.[17] The transient absorption spectra in the 500–750 nm range showed the signals of MIL-125 rapidly decayed to the ground state and were accompanied by a negative absorption of stimulated emission (< 525 nm) (Figure 22a). In contrast, MIL-125-NH_2 displayed an intense and broad transient signal (Figure 22b). The kinetics plots clearly indicated the much longer charge lifetime of MIL-125-NH_2 than that of MIL-125 (Figure 22c). Furthermore, TAS in

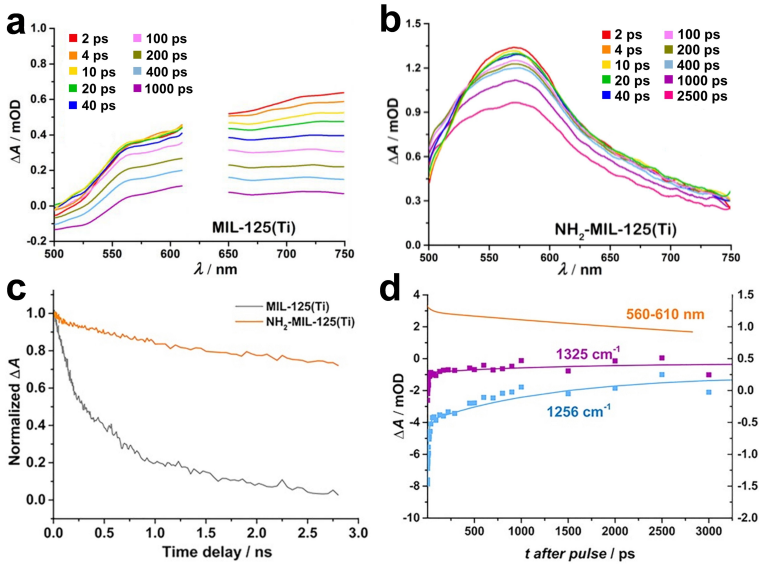

Figure 22. The TAS of (a) MIL-125 and (b) MIL-125-NH_2. (c) The kinetic plots of MIL-125 and MIL-125-NH_2 in the range of 560–610 nm. (d) The kinetic plots of the visible region (orange), C–C (purple) and C–N stretching vibration (blue) for MIL-125-NH_2. Adapted with permission.[17] Copyright 2016, Wiley-VCH.

the IR region was performed to trace the kinetics of holes (on linkers) through probing the vibrations of organic groups in linkers. The feature signals of -NH_2 group in MIL-125-NH_2 were recorded. Compared to the asymmetrical N–H stretching vibration, a more obvious redshift transient signal of symmetrical N–H stretching vibration indicated the production of positive aniline radical in the BDC-NH_2 linker. The slower decay of the amino-related C–N signal (1256 cm^{-1}) than the C–C stretching vibration (1325 cm^{-1}) further supported the hole stabilizing effect of -NH_2 (Figure 22d).

5.2. X-ray Absorption Spectroscopy

Although TAS allows us to understand the kinetic behavior of photocatalysts from fs to μs scales, it is hard to accurately determine the direction of charge transfer, i.e. the process of electron transfer from photosensitizer to catalytic site. Given the well-defined light antenna and active sites in MOFs, in situ X-ray absorption spectroscopy (XAS) is applied in combination with TAS to elucidate the relationship between the structural evolution of catalytic centers and charge transfer kinetics, by which the direction of electron transfer can be determined.[69] Particularly, a representative photocatalytic H_2 production system of Co-Ru-UiO-67 containing a Ru-based photosensitizer and Co-based catalytic sites was fabricated to reveal the intermediate species and reaction dynamics via in situ XAS and fs-TAS (Figure 23a).[69b] The fs-TAS results first confirmed the charge separation process via electron transfer from the Ru complex to the Co sites, where the electron transfer process is much faster than the charge recombination process together with the formation of transient Co intermediates for photocatalysis (Figure 23b). To establish the relationship between the evolution process of Co intermediates and the electron transfer process, in situ XAS was conducted to collect the structural information of Co intermediates. The in situ X-ray absorption near-edge structure (XANES) spectra showed a remarkable red-shift in both region I (edge) and region II (above-edge oscillations) (Figure 23c). The edge shift to lower energy indicated the reduction of Co^{2+} to Co^{+}, while the shift of above-edge oscillations manifested the enlarged Co-L bonds (L is coordinating atom). After turning off the light, the changed XANES spectra were recovered to their original state, indicating that these signal changes were not from catalyst degradation. Furthermore, the Fourier-transformed X-ray absorption fine structure (XAFS) spectra confirmed that the reduction process of Co^{2+} to Co^{+} was ascribed to the enlarged Co-L bonds to Co-N (1.98 Å to 2.11 Å) and Co-Cl (2.25 Å to 2.28 Å) bonds in the first shell (Figure 23d). This work disclosed the formation of a long-lived Co^{+} intermediate in photocatalytic H_2 production, which originated from the electron transfer process from the Ru photosensitizer to Co sites.

5.3. Kelvin Probe Force Microscopy

Kelvin probe force microscopy (KPFM) is a technique to measure the contact potential difference (CPD) between the probe tip and sample surface, which can reflect the surface work function of photocatalysts.[70] Recently, the in situ photon-irradiated KPFM technique has been employed to disclose the spatial location of the photogenerated electrons and holes in photocatalysis, where the surface photovoltage (SPV) can be collected by measuring the

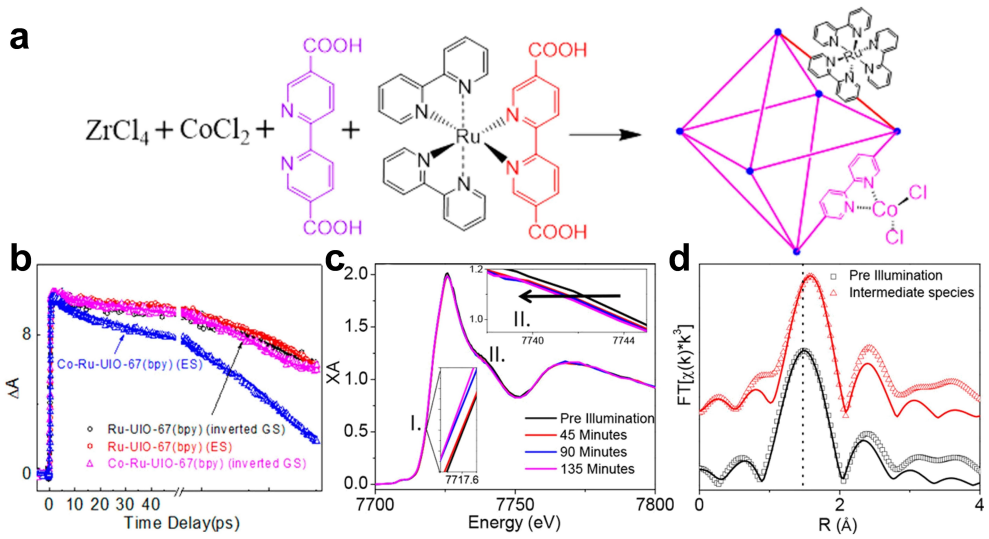

Figure 23. (a) Synthetic scheme of Co-Ru-UiO-67. (b) The kinetic plots of Ru-UiO-67 and Co-Ru-UiO-67. (c) The in situ XANES spectra of Co-Ru-UiO-67 before and after light irradiation. (d) Fourier-transformed XAFS spectra of Co-Ru-UIO-67 before and after light irradiation. Adapted with permission.[69b] Copyright 2018, American Chemical Society.

CPD change under light irradiation, thereby realizing the space-resolution of charge kinetics.[68b,70a]

Recently, Ma and co-workers investigated the spatial charge distribution in a MOF homojunction with the help of in situ photon-irradiated KPFM.[70b] In this work, they developed a "transition metal NPs-directed MOF growth" strategy to synthesize a MOF composite composed of concentric MOF(s)/MOF(l) nanoplates (Figure 24a and 24b). The two stacked MOF nanoplates showed different energy levels due to the different chemical compositions and crystal structures, leading to a homojunction interface (Figure 24c). The homojunction composite resulted in a better CO_2 photoreduction activity than the single MOF counterpart. To visualize the charge separation in the homojunction structure, the in situ photon-irradiated KPFM was carried out. In the dark, the small MOF(s) showed a lower CPD signal than the large MOF(l) due to the higher surface work function of the MOF(s) (Fig-

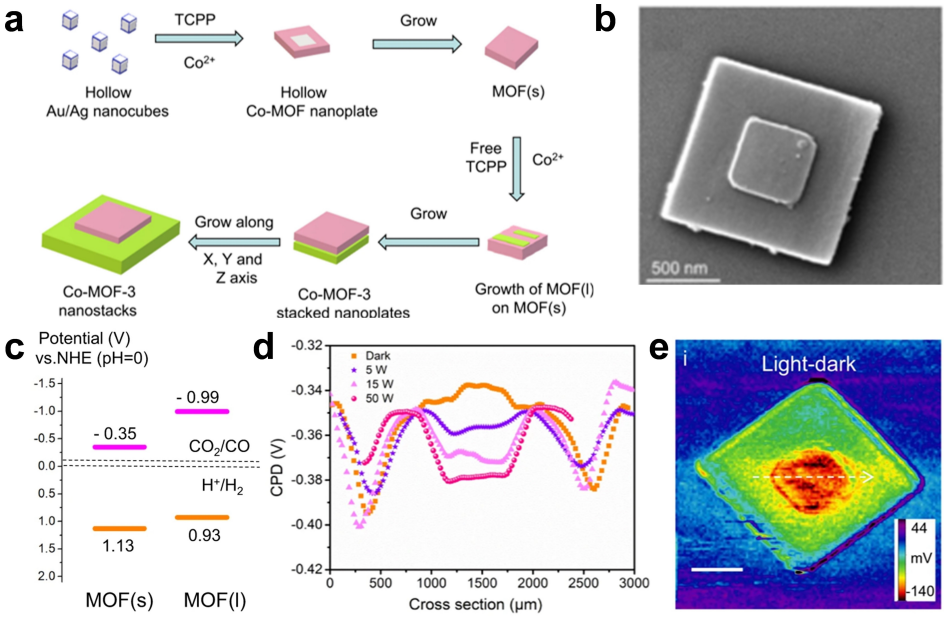

Figure 24. (a) Schematic diagram of the procedure to prepare MOF homojunction. (b) The image of MOF homojunction. (c) The energy diagram of MOF homojunction. (d) The CPD signal in the dark and under light irradiation. (e) The SPV image of MOF homojunction obtained by subtracting the potential in the dark from that under 50 W light irradiation. Adapted with permission.[70b] Copyright 2021, Nature Publishing Group.

ure 24d). Upon light on, a more negative SPV signal was observed in MOF(s) than in MOF(l) (Figure 24e). The opposite SPV signals demonstrated the electrons accumulated on the surface of MOF(s) yet holes migrated to the MOF(l), which further supported the existence of homojunction. Apart from the homojunction, the charge distribution on the heterojunction between atomic-layer Fe_2O_3 and 2D Zn-TCPP was revealed by in situ photon-irradiated KPFM.[70c]

5.4. Diffuse Reflectance Infrared Fourier Transform Spectroscopy

Diffuse reflectance infrared Fourier transform spectroscopy (DRIFTS) is an analytical technique for collecting diffuse scattered signals from infrared radiation on powders. DRIFTS provides an approach to probe the structural information of photocatalysts and reaction intermediates.[68a,71] In terms of MOFs, DRIFTS has been developed to assess the electron states and coordination microenvironment of catalytic sites, detect the structural transformation of MOFs, determine the cluster defect sites and the modified species, and trace the reaction intermediates, and so on.[42b,43a,44f,72]

DRIFTS is recognized as an important tool for the detection of CO_2 reduction intermediates to disclose the catalytic mechanism. Maji and co-workers investigated the reaction mechanisms in the photoreduction of CO_2 to CO over Zr-MBA-Ru/Re-MOF.[72d] After introducing CO_2 and H_2O into the system, the monodentate carbonate group (m-CO_3^{2-}) appeared at 1314 and 1509 cm^{-1}, which originated from the reaction of CO_2 and H_2O. Upon light irradiation, the crucial intermediate COOH* for CO_2 to CO gradually enhanced at 1620 cm^{-1} accompanied by the formation of CO*(2060 cm^{-1}) (Figure 25a). Based on these intermediates, the proposed catalytic path is illustrated (Figure 25b).

Although DRIFTS represents a powerful tool to capture reaction intermediates, it should be noted that some detected intermediates by DRIFTS spectroscopy could not be involved in the reaction mechanism.[72e] Therefore, the reliable mechanism should be based on the combined analysis of DRIFTS results together with other related data.

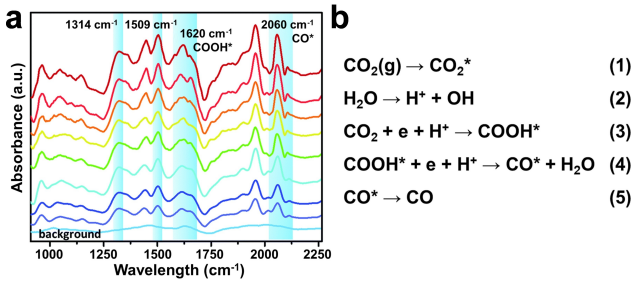

Figure 25. (a) The in situ DRIFT spectra and (b) proposed mechanism of CO_2 photoreduction over Zr-MBA-Ru/Re-MOF. Adapted with permission.[72d] Copyright 2021, The Royal Society of Chemistry.

5.5. Electron Paramagnetic Resonance Spectroscopy

Electron paramagnetic resonance (EPR) spectroscopy is a technique to detect the unpaired electrons in molecules or solid materials. The EPR signals originate from the resonance transitions between the energy levels of electron spins under static magnetic field, which is highly sensitive to the geometric structure and chemical microenvironment of paramagnetic species. In particular, many paramagnetic species, such as transition metal ions, active radicals, etc., are involved in catalytic reactions.[73] Currently, EPR spectroscopy has been widely applied to diversified catalytic systems.

In addition to the signals from reaction intermediates, there are many transient paramagnetic signals in MOFs accompanied with the gain or loss of electrons of organic linkers and metal nodes during the photocatalytic process. Based on these transient signals, we can propose charge transfer and catalytic mechanism.[74] Typically, Yan et al. developed a dinuclear Eu^{III}_2 MOF for photocatalytic CO_2 reduction (Figure 26a).[74a] In situ EPR experiments were performed to reveal the photoinduced electron transfer process (Figure 26b). Under irradiation with visible light, a broad and a weak EPR signals can be observed at g = 2.23 and 4.61, respectively, which can be assigned to Eu^{2+} metal species. When CO_2 was introduced into the system, the EPR signal of Eu^{2+} was strongly suppressed due to electron transfer from Eu^{2+} to CO_2. This work proved the LMCT process in MOF photocatalysis by EPR signals from reduced metal species; however, the oxidized linker signals corresponding to the holes are unclear. In another work, direct evidence of photogenerated electrons and holes

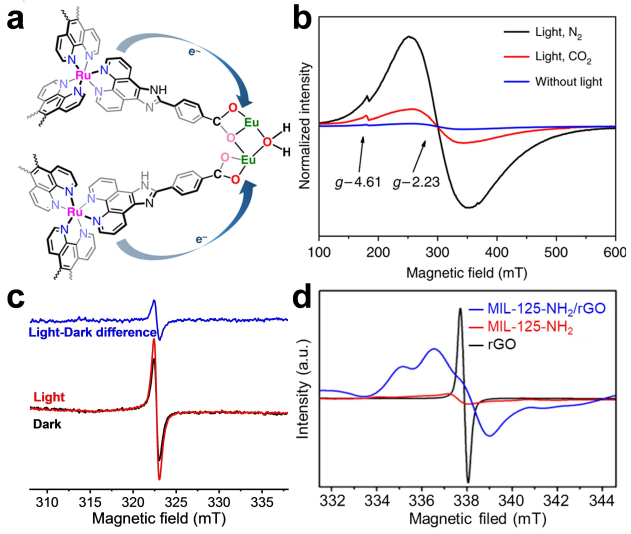

Figure 26. (a) Schematic charge transfer process in the dinuclear Eu^{III}_2 MOF. (b) EPR spectra of Eu-MOF under different conditions. Adapted with permission.[74a] Copyright 2018, Nature Publishing Group. (c) EPR signals related to porphyrin π-cation radical in PCN-222. Adapted with permission.[13] Copyright 2018, The Royal Society of Chemistry. (d) EPR spectra of rGO, MIL-125-NH_2, and MIL-125-NH_2/rGO. Adapted with permission.[74b] Copyright 2018, American Chemical Society.

produced via LMCT process was clearly obtained by EPR spectroscopy.[13] PCN-222 is a representative porphyrinic MOF in which an enhanced porphyrin π-cation radical signal was detected by EPR under illumination (Figure 26c), while the EPR signal for the homogeneous porphyrin molecule gave no apparent change. The porphyrin π-cation radical signal unambiguously demonstrated that the photogenerated holes were located on the ligand, supporting the LMCT process.

The interactions between composite photocatalysts are important for enhanced photocatalytic performance. The π-π interaction between reduced graphene oxide (rGO) and MIL-125-NH_2 was confirmed by EPR.[74b] Compared with the EPR signals of MIL-125-NH_2 and rGO, the composite signal was significantly broadened and accompanied by splitting and displacement (Figure 26d). This phenomenon was attributed to the extended delocalization and rapid spin-lattice relaxation of the π-electrons in rGO, as well as the enhanced spin-orbital coupling between rGO and MIL-125-NH_2.

Although EPR spectroscopy is widely applied into catalytic studies, the limitations should be noted. Firstly, its time-resolution within 10 ns is not sufficient to detect some intermediates.[73b] To solve this, spin trap reagents and low-temperature experiments, such as using 5,5-dimethyl-1-pyrroline N-oxide (DMPO) to capture ·OH, might be helpful. Secondly, quantification is difficult in EPR, where signal intensity is affected by many factors including spin state, relaxation times, experimental parameters and so on. Thus, accurate quantification depends on standard samples, but most standard samples are not readily available.[73a]

5.6. X-ray Photoelectron Spectroscopy

When X-ray irradiates the surface of materials, the X-ray photons can be absorbed by the inner electrons of materials, causing the electrons to escape the constraint of the nucleus and become free photoelectrons. The energy of photoelectrons is highly dependent on the type of element and the chemical states. X-ray photoelectron spectroscopy (XPS) is an analytic approach to measure the kinetic energy of photoelectrons, which has become one of the most widely used tools in catalytic studies.[68,75]

In addition to providing information about the elemental composition and chemical state in the catalysts, XPS has been developed to investigate charge transfer in photocatalysis. Specifically, Lan and co-workers fabricated a COF-318-TiO_2 photocatalyst for CO_2 photoreduction.[75b] Band analysis indicated that the charge transfer pathway in the composites could obey a Z-scheme mechanism (Figure 27a). To support the Z-scheme mechanism, in situ XPS was conducted to reveal the direction of electron flow. Under light irradiation, a positive shift of Ti 2p binding energy was observed (Figure 27b), which manifested the decrease in electron density at Ti sites, supporting the Z-scheme mechanism that the electrons might flow from TiO_2 to COF-318. Similarly, the S-scheme heterojunction

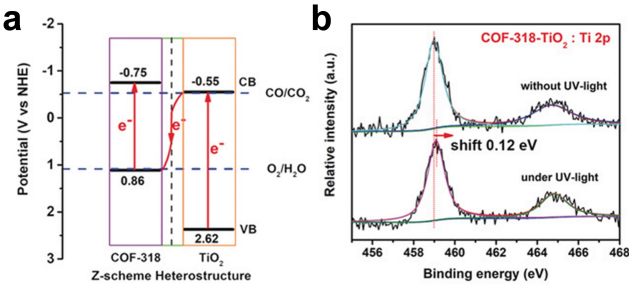

Figure 27. (a) The Z-scheme electron transfer mechanism in COF-318-TiO_2. (b) The in situ XPS for Ti 2p of COF-318-TiO_2 in the dark and under light. Adapted with permission.[75b] Copyright 2020, Wiley-VCH.

over NH_2-UiO-66@DAT-HOF was evidenced by in situ XPS.[75c]

6. Summary

In this review, we first introduce the semiconductor-like behavior of MOFs, and summarize the recent advances on photocatalytic water splitting and CO_2 reduction over MOFs. To understand the photocatalytic mechanism, the time- and space-resolved techniques of TAS and KPFM, as well as XAS, DRIFTS, EPR, and XPS for tracing reaction intermediates and mechanisms are discussed. Although the present reports demonstrate the great potential of MOFs in photocatalytic water splitting and CO_2 reduction, the challenges exist and further efforts need to be made for further development in this field.

Firstly, the evolution rate, such as μmol/gh, is widely used to present the photocatalytic activity in MOF photocatalysis. However, rate is usually influenced by light source, catalyst amount, temperature, pressure, etc. In this regard, AQE, i.e., the efficiency based on photon number, may be a better metric.[76] In addition, photocatalytic water splitting and CO_2 reduction over MOFs mostly occur in the presence of sacrificial agents, which greatly limits their practical application and produces unwanted waste. Sacrificial agents are also unfavorable to MOF stability. Typically, carboxylate MOFs are unstable to the alkalinity of amines, such as triethylamine, the most commonly used sacrificial agents in MOF photocatalysis. For water splitting, although MOFs for photocatalytic OWS have been reported sporadically, the reproducibility remains to be examined and there is a lack of rational guidance on catalyst design. Regarding CO_2 reduction, although the overall CO_2 reduction seems more workable in a gas-solid mode, great efforts should be devoted to improving the activity and the value of products. Recently, the piezoelectric effect has presented potential in promoting MOF photocatalysis.[77] The external field can accelerate charge directional migration and affect the charge spatial distribution, which might be an attractive strategy to enhanced photocatalysis.

Secondly, catalyst stability remains a concern for MOF photocatalysis. Particularly, the long-term photostability of MOFs should be noticed. It was reported that carboxylate

MOFs undergo photodecarboxylation, whose porosity and surface area have changed, while XRD and some routine characterizations cannot definitely show their decomposition.[78] Moreover, the decomposition of solvent and carbon residues sometimes leads to false positive activity.[79] The ^{13}C-labeled technique is usually adopted to determine the origin of carbon products in CO_2 photoreduction, but there are some issues worth noting,[80] such as partial molecular ion peaks only, the mismatch between the intensity of total ion flow and the total molecular ion peaks, and mismatch of the ratio of ^{13}C and ^{16}O fragments, which might result in false positive results. For example, a typical ^{13}C-labeled CO mass spectrum was reported in many photocatalytic CO_2 literatures (Figure 28). However, there are some potential puzzles in this spectrum. Mass spectrum is a technique for detecting the fragments of a molecule, in which the ^{13}CO peak may originate from the fragment of $^{13}CO_2$. Meanwhile, the molar ratio of C and O in CO is 1, whereas the signal of ^{16}O is much higher than ^{13}C in this spectrum, which more likely comes from $^{13}CO_2$ (the molar ratio of O and C is 2). In brief, this kind of spectrum possibly show the fragment of $^{13}CO_2$ rather than ^{13}CO. Similarly, in photocatalytic water oxidation, the sacrificial agents of persulfates potentially behave as an oxo-transfer reagent, leading to additional O_2 rather than producing from H_2O. The source of the oxygen atoms in the O_2 should be determined by using $H_2{}^{18}O$.[81]

Last, the organic groups of MOFs lead to background noise and poor reproducibility in characterization, e.g. DRIFTS, Raman spectroscopy, which interferes with the investigation on the reaction mechanism. Also, the irradiation stability of some MOFs is poor due to the weak coordination bonding. In this case, it is unfavorable to use the common in situ spectroscopy and electron microscopy characterizations.[82] It is essential for the development of more sensitive and nondestructive characterization techniques.

Given the atomically precise and tailorable structures, MOFs show high customizability in light adsorption, redox ability, and catalytic sites, which offer excellent compatibility with various photocatalytic reactions and provide a powerful platform for investigating structure-performance relationships in photocatalysis. Here we propose some prospects for the possible future development of MOF photocatalysis.

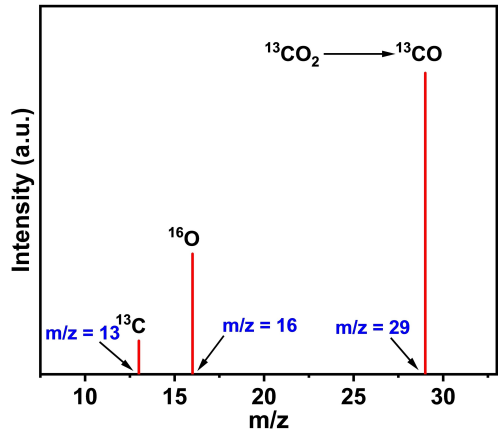

Figure 28. A typical questionable mass spectrum demonstrating the production of ^{13}CO from $^{13}CO_2$.

a) The LMCT process is currently an almost universal principle for designing MOF photocatalysts that can greatly promote charge separation.[9a–f] The LMCT process relies heavily on open-shell metal nodes, which presents two sides—the open-shell metal nodes not only behave as the channels of electron transfer but also possibly serve as the centers for the recombination of electrons and holes.[83] Recently, the LLCT, MLCT, and MMCT processes have shown potential advantages in photocatalysis.[21b,c,84] These different charge transfer processes may overcome the drawbacks of LMCT in specific application scenarios. For example, MTV-MIL-100 exhibited a high photocatalytic activity in NH_3BH_3 hydrolysis via a MMCT process, which is superior to MIL-125 featuring LMCT process.[84]

b) Compared to conventional photocatalysts, MOFs present their particular advantages. The variety of organic linkers and metal nodes endow MOFs with more tunable structures and physicochemical properties. More importantly, given the structural tailorability and compatibility of MOFs, the active sites can be rationally installed/manipulated to achieve synergistic catalysis and tandem catalysis toward highly valuable products in CO_2 photoreduction. The recent tandem catalysis of CO_2 to carbonylation through CO intermediate seems to be a promising strategy.[62b,c] In addition, the unique stimuli responsiveness and the flexible backbone of MOFs will lead to different host-guest interactions.[85] Meanwhile, based on the atomically precise structure of MOFs in combination with advanced characterization techniques, we can unambiguously elucidate the structural evolution of active units and explore the influence of the microenvironment around catalytic sites on photocatalysis.[86]

c) Up to now, there have been more than 90000 kinds of MOFs, while over 500000 structures have been predicted with the aid of computer science.[87] In most cases, the metal nodes of MOFs are metal ions/clusters. Recently, polyoxometalates[88] and organolead halide hybrids[89] have been developed to coordinate with organic linkers to construct MOFs. The polyoxometalate-based MOFs exhibit a stronger redox ability for the photoreduction of CO_2 to CH_4, and the latter enables enhanced carrier mobility, which inspires us to adopt diverse clusters to develop new MOFs. It should be noted that the emerging artificial intelligence (AI) and big data techniques would be powerful tools in the on-demand synthesis of MOFs.[90]

d) It is a challenge for conventional semiconductors to drive photocatalysis under infrared (IR) light that is composed of ≈50% of the solar spectrum. MOFs would be better candidates for harnessing IR light due to the tunable organic linkers. Recently, Zeng et al. designed a series of porphyrin-based MOFs with different π-electrons for CO_2 photoreduction, the light adsorption range of which

can be modulated from visible to IR light. The optimal MOF can reduce CO_2 to HCOOH with a remarkable AQE of 1.11 % under IR light irradiation.[21d] Incorporation of guest species is another way to extend light harvesting of MOFs to the IR region for photocatalysis.[23d] However, it should be noted that the excitation energy of IR light is low, making it hard to drive the reactions with high redox potentials. The photothermal effect of IR light could be an alternative solution, where the "hot spots" around catalytic sites can greatly accelerate the reaction.[72c,91]

e) An overall reaction without sacrificial agents remains the goal in photocatalysis, yet the sluggish water oxidation reaction is hard to overcome. Dual-functional photocatalysis was reported to meet this challenge, where dye degradation and/or organic oxidation to valuable chemicals were adopted to couple with photocatalytic H_2 production and CO_2 reduction instead of simply consuming sacrificial agents, providing a more sustainable strategy.[92]

f) At present, most photocatalytic CO_2 reduction experiments are conducted under pure CO_2; however, the real CO_2 emitted from real industrial processes is at a low concentration and contains O_2 that quenches reduction reaction immediately. MOFs exhibit the potential to achieve low concentration CO_2 photoreduction,[63] yet related studies are still preliminary and further advances are expected to achieve photocatalytic CO_2 reduction under oxygenated conditions. More importantly, MOFs can be fabricated into devices, e.g. membranes; MOFs possess low density, high surface areas, high porosity and well-controllable structures, which would be favorable to the direct adsorption of CO_2 from gas phase in real industrial applications.[26c,50c]

In summary, while research on photocatalysis has been ongoing for over half a century, the study of MOFs for photocatalysis is in its infancy. Undoubtedly, the high surface area, compatible, well-defined and tailorable structures of MOFs are very important strengths toward photocatalysis. We are confident that MOFs will not only provide deeper insights into photocatalysis, but also guide to the development of efficient photocatalysts for water splitting and CO_2 reduction.

Acknowledgements

This work was supported by the National Key Research and Development Program of China (2021YFA1500400), National Natural Science Foundation of China (U22A20401, 21725101, 22161142001), and International Partnership Program of CAS (123GJHZ2022028MI).

Conflict of Interest

The authors declare no conflict of interest.

Keywords: Advanced Characterizations · CO_2 Reduction · Metal-Organic Frameworks · Photocatalysis · Water Splitting

[1] S. Chu, Y. Cui, N. Liu, *Nat. Mater.* **2017**, *16*, 16–22.
[2] J. Marshall, *Nature* **2014**, *510*, 22–24.
[3] J. Z. Zhang, E. Reisner, *Nat. Chem. Rev.* **2020**, *4*, 6–21.
[4] Q. Wang, K. Domen, *Chem. Rev.* **2020**, *120*, 919–985.
[5] a) Y.-J. Yuan, Z.-T. Yu, D.-Q. Chen, Z.-G. Zou, *Chem. Soc. Rev.* **2017**, *46*, 603–631; b) B. Zhang, L. Sun, *Chem. Soc. Rev.* **2019**, *48*, 2216–2264.
[6] a) X. Meng, L. Liu, S. Ouyang, H. Xu, D. Wang, N. Zhao, J. Ye, *Adv. Mater.* **2016**, *28*, 6781–6803; b) G. Zhang, Z. A. Lan, X. Wang, *Angew. Chem. Int. Ed.* **2016**, *55*, 15712–15727; *Angew. Chem.* **2016**, *128*, 15940–15956; c) X. Liu, S. Inagaki, J. Gong, *Angew. Chem. Int. Ed.* **2016**, *55*, 14924–14950; *Angew. Chem.* **2016**, *128*, 15146–15174; d) A. Meng, L. Zhang, B. Cheng, J. Yu, *Adv. Mater.* **2019**, *31*, 1807660.
[7] a) H. Furukawa, K. E. Cordova, M. O'Keeffe, O. M. Yaghi, *Science* **2013**, *341*, 1230444; b) H.-C. Zhou, S. Kitagawa, *Chem. Soc. Rev.* **2014**, *43*, 5415–5418; c) Y. Cui, B. Li, H. He, W. Zhou, B. Chen, G. Qian, *Acc. Chem. Res.* **2016**, *49*, 483–493; d) H. Li, L. Li, R.-B. Lin, W. Zhou, Z. Zhang, S. Xiang, B. Chen, *EnergyChem* **2019**, *1*, 100006; e) G. Cai, P. Yan, L. Zhang, H.-C. Zhou, H.-L. Jiang, *Chem. Rev.* **2021**, *121*, 12278–12326; f) X. Zhao, Y. Wang, D.-S. Li, X. Bu, P. Feng, *Adv. Mater.* **2018**, *30*, 1705189.
[8] a) A. Corma, H. García, F. X. Llabrés i Xamena, *Chem. Rev.* **2010**, *110*, 4606–4655; b) H. Zhang, J. Nai, L. Yu, X. W. Lou, *Joule* **2017**, *1*, 77–107; c) Y.-B. Huang, J. Liang, X.-S. Wang, R. Cao, *Chem. Soc. Rev.* **2017**, *46*, 126–157; d) G. Li, S. Zhao, Y. Zhang, Z. Tang, *Adv. Mater.* **2018**, *30*, 1800702; e) L. Jiao, H.-L. Jiang, *Chem* **2019**, *5*, 786–804; f) Q. Wang, D. Astruc, *Chem. Rev.* **2020**, *120*, 1438–1511; g) Y. Shen, T. Pan, L. Wang, Z. Ren, W. Zhang, F. Huo, *Adv. Mater.* **2021**, *33*, 2007442; h) Y.-S. Wei, M. Zhang, R. Zou, Q. Xu, *Chem. Rev.* **2020**, *120*, 12089–12174; i) J. Liu, T. A. Goetjen, Q. Wang, J. G. Knapp, M. C. Wasson, Y. Yang, Z. H. Syed, M. Delferro, J. M. Notestein, O. K. Farha, J. T. Hupp, *Chem. Soc. Rev.* **2022**, *51*, 1045–1097.
[9] a) T. Zhang, W. Lin, *Chem. Soc. Rev.* **2014**, *43*, 5982–5993; b) J.-D. Xiao, H.-L. Jiang, *Acc. Chem. Res.* **2019**, *52*, 356–366; c) X. Li, Q.-L. Zhu, *EnergyChem* **2020**, *2*, 100033; d) T. Zhang, Y. Jin, Y. Shi, M. Li, J. Li, C. Duan, *Coord. Chem. Rev.* **2019**, *380*, 201–229; e) J. Zhu, P.-Z. Li, W. Guo, Y. Zhao, R. Zou, *Coord. Chem. Rev.* **2018**, *359*, 80–101; f) D. Li, M. Kassymova, X. Cai, S.-Q. Zang, H.-L. Jiang, *Coord. Chem. Rev.* **2020**, *412*, 213262; g) A. Dhakshinamoorthy, Z. Li, H. Garcia, *Chem. Soc. Rev.* **2018**, *47*, 8134–8172; h) L. Cao, C. Wang, *ACS Cent. Sci.* **2020**, *6*, 2149–2158.
[10] a) L. Łukasiak, A. Jakubowski, *J. Telecommun. Inf. Technol.* **2010**, *1*, 3–9; b) T. Jenkins, *Phys. Educ.* **2005**, *40*, 430.
[11] J. Shi, J. Zhang, L. Yang, M. Qu, D. C. Qi, K. H. L. Zhang, *Adv. Mater.* **2021**, *33*, 2006230.
[12] C. G. Silva, A. Corma, H. García, *J. Mater. Chem.* **2010**, *20*, 3141–3156.
[13] C. Xu, H. Liu, D. Li, J.-H. Su, H.-L. Jiang, *Chem. Sci.* **2018**, *9*, 3152–3158.
[14] C. Zhang, C. Xie, Y. Gao, X. Tao, C. Ding, F. Fan, H.-L. Jiang, *Angew. Chem. Int. Ed.* **2022**, *61*, e202204108; *Angew. Chem.* **2022**, *134*, e202204108.
[15] S. E. Braslavsky, A. M. Braun, A. E. Cassano, A. V. Emeline, M. I. Litter, L. Palmisano, V. N. Parmon, N. Serpone, *Pure Appl. Chem.* **2011**, *83*, 931–1014.
[16] M. Usman, S. Mendiratta, K. L. Lu, *Adv. Mater.* **2017**, *29*, 1605071.

[17] J. G. Santaclara, M. A. Nasalevich, S. Castellanos, W. H. Evers, F. C. Spoor, K. Rock, L. D. Siebbeles, F. Kapteijn, F. Grozema, A. Houtepen, J. Gascon, J. Hunger, M. A. van der Veen, *ChemSusChem* **2016**, *9*, 388–395.

[18] J. Long, S. Wang, Z. Ding, S. Wang, Y. Zhou, L. Huang, X. Wang, *Chem. Commun.* **2012**, *48*, 11656–11658.

[19] a) X. P. Wu, L. Gagliardi, D. G. Truhlar, *J. Am. Chem. Soc.* **2018**, *140*, 7904–7912; b) M. A. Syzgantseva, C. P. Ireland, F. M. Ebrahim, B. Smit, O. A. Syzgantseva, *J. Am. Chem. Soc.* **2019**, *141*, 6271–6278.

[20] N. Kolobov, M. G. Goesten, J. Gascon, *Angew. Chem. Int. Ed.* **2021**, *60*, 26038–26052; *Angew. Chem.* **2021**, *133*, 26242–26256.

[21] a) D. Feng, Z. Y. Gu, J. R. Li, H.-L. Jiang, Z. Wei, H. C. Zhou, *Angew. Chem. Int. Ed.* **2012**, *51*, 10307–10310; *Angew. Chem.* **2012**, *124*, 10453–10456; b) M. Elcheikh Mahmoud, H. Audi, A. Assoud, T. H. Ghaddar, M. Hmadeh, *J. Am. Chem. Soc.* **2019**, *141*, 7115–7121; c) C. Xu, Y. Pan, G. Wan, H. Liu, L. Wang, H. Zhou, S. H. Yu, H.-L. Jiang, *J. Am. Chem. Soc.* **2019**, *141*, 19110–19117; d) J.-Y. Zeng, X.-S. Wang, B.-R. Xie, Q.-R. Li, X.-Z. Zhang, *J. Am. Chem. Soc.* **2022**, *144*, 1218–1231; e) F. Leng, H. Liu, M. Ding, Q.-P. Lin, H.-L. Jiang, *ACS Catal.* **2018**, *8*, 4583–4590.

[22] a) X. Guo, L. Liu, Y. Xiao, Y. Qi, C. Duan, F. Zhang, *Coord. Chem. Rev.* **2021**, *435*, 213785; b) A. S. Yasin, J. Li, N. Wu, T. Musho, *Phys. Chem. Chem. Phys.* **2016**, *18*, 12748–12754.

[23] a) Q. Yang, Q. Xu, H.-L. Jiang, *Chem. Soc. Rev.* **2017**, *46*, 4774–4808; b) Q.-L. Zhu, Q. Xu, *Chem. Soc. Rev.* **2014**, *43*, 5468–5512; c) Y. Li, M. Karimi, Y.-N. Gong, N. Dai, V. Safarifard, H.-L. Jiang, *Matter* **2021**, *4*, 2230–2265; d) D. Li, S. H. Yu, H.-L. Jiang, *Adv. Mater.* **2018**, *30*, 1707377; e) Z.-X. Sun, K. Sun, M.-L. Gao, Ö. Metin, H.-L. Jiang, *Angew. Chem. Int. Ed.* **2022**, *61*, e202206108; *Angew. Chem.* **2022**, *134*, e202206108; f) Y. Pan, Y. Qian, X. Zheng, S.-Q. Chu, Y. Yang, C. Ding, X. Wang, S.-H. Yu, H.-L. Jiang, *Natl. Sci. Rev.* **2021**, *8*, nwaa224.

[24] H. Liu, H. Ma, J. Joo, Y. Yin, *Sci. China Mater.* **2016**, *59*, 1017–1026.

[25] M. Li, D. Xia, Y. Yang, X. Du, G. Dong, A. Jiang, R. Fan, *Adv. Energy Mater.* **2018**, *8*, 1702052.

[26] a) V. Stavila, A. A. Talin, M. D. Allendorf, *Chem. Soc. Rev.* **2014**, *43*, 5994–6010; b) G. Paille, M. Gomez-Mingot, C. Roch-Marchal, M. Haouas, Y. Benseghir, T. Pino, M. H. Ha-Thi, G. Landrot, P. Mialane, M. Fontecave, A. Dolbecq, C. Mellot-Draznieks, *ACS Appl. Mater. Interfaces* **2019**, *11*, 47837–47845; c) Y.-C. Hao, L.-W. Chen, J. Li, Y. Guo, X. Su, M. Shu, Q. Zhang, W.-Y. Gao, S. Li, Z.-L. Yu, L. Gu, X. Feng, A.-X. Yin, R. Si, Y.-W. Zhang, B. Wang, C.-H. Yan, *Nat. Commun.* **2021**, *12*, 2682.

[27] a) L. Zhang, H. H. Mohamed, R. Dillert, D. Bahnemann, *J. Photochem. Photobiol. C* **2012**, *13*, 263–276; b) S. Corby, R. R. Rao, L. Steier, J. R. Durrant, *Nat. Rev. Mater.* **2021**, *6*, 1136–1155.

[28] C. Gomes Silva, I. Luz, F. X. Llabres i Xamena, A. Corma, H. Garcia, *Chem. Eur. J.* **2010**, *16*, 11133–11138.

[29] a) J. Yang, D. Wang, H. Han, C. Li, *Acc. Chem. Res.* **2013**, *46*, 1900–1909; b) J. Ran, J. Zhang, J. Yu, M. Jaroniec, S. Z. Qiao, *Chem. Soc. Rev.* **2014**, *43*, 7787–7812.

[30] Y. Kataoka, K. Sato, Y. Miyazaki, K. Masuda, H. Tanaka, S. Naito, W. Mori, *Energy Environ. Sci.* **2009**, *2*, 397–400.

[31] a) K. Meyer, M. Ranocchiari, J. A. van Bokhoven, *Energy Environ. Sci.* **2015**, *8*, 1923–1937; b) K. Zhang, H. Hu, L. Shi, B. Jia, H. Huang, X. Han, X. Sun, T. Ma, *Small Sci.* **2021**, *1*, 2100060; c) Y. Horiuchi, T. Toyao, M. Saito, K. Mochizuki, M. Iwata, H. Higashimura, M. Anpo, M. Matsuoka, *J. Phys. Chem. C* **2012**, *116*, 20848–20853; d) D. Sun, W. Liu, Y. Fu, Z. Fang, F. Sun, X. Fu, Y. Zhang, Z. Li, *Chem. Eur. J.* **2014**, *20*, 4780–4788; e) S.-Y. Han, D.-L. Pan, H. Chen, X.-B. Bu, Y.-X. Gao, H. Gao, Y. Tian, G.-S. Li, G. Wang, S.-L. Cao, C.-Q. Wan, G.-C. Guo, *Angew. Chem. Int. Ed.* **2018**, *57*, 9864–9869; *Angew. Chem.* **2018**, *130*, 10012–10017; f) A. Fateeva, P. A. Chater, C. P. Ireland, A. A. Tahir, Y. Z. Khimyak, P. V. Wiper, J. R. Darwent, M. J. Rosseinsky, *Angew. Chem. Int. Ed.* **2012**, *51*, 7440–7444; *Angew. Chem.* **2012**, *124*, 7558–7562; g) N. M. Padial, J. Castells-Gil, N. Almora-Barrios, M. Romero-Angel, I. da Silva, M. Barawi, A. Garcia-Sanchez, V. A. de la Pena O'Shea, C. Marti-Gastaldo, *J. Am. Chem. Soc.* **2019**, *141*, 13124–13133; h) Y. Xiao, Y. Qi, X. Wang, X. Wang, F. Zhang, C. Li, *Adv. Mater.* **2018**, *30*, 1803401; i) J.-D. Xiao, L. Han, J. Luo, S.-H. Yu, H.-L. Jiang, *Angew. Chem. Int. Ed.* **2018**, *57*, 1103–1107; *Angew. Chem.* **2018**, *130*, 1115–1119; j) S. Yuan, J.-S. Qin, H.-Q. Xu, J. Su, D. Rossi, Y. Chen, L. Zhang, C. Lollar, Q. Wang, H.-L. Jiang, D.-H. Son, H. Xu, Z. Huang, X. Zou, H.-C. Zhou, *ACS Cent. Sci.* **2018**, *4*, 105–111; k) X. Ma, L. Wang, Q. Zhang, H.-L. Jiang, *Angew. Chem. Int. Ed.* **2019**, *58*, 12175–12179; *Angew. Chem.* **2019**, *131*, 12303–12307.

[32] a) J. He, J. Wang, Y. Chen, J. Zhang, D. Duan, Y. Wang, Z. Yan, *Chem. Commun.* **2014**, *50*, 7063–7066; b) J. Shi, F. Chen, L. Hou, G. Li, Y. Li, X. Guan, H. Liu, L. Guo, *Appl. Catal. B* **2021**, *280*, 119385.

[33] a) J. He, Z. Yan, J. Wang, J. Xie, L. Jiang, Y. Shi, F. Yuan, F. Yu, Y. Sun, *Chem. Commun.* **2013**, *49*, 6761–6763; b) H.-Q. Xu, S. Yang, X. Ma, J. Huang, H.-L. Jiang, *ACS Catal.* **2018**, *8*, 11615–11621; c) Y. Wang, Z. Zhang, J. Li, Y. Yuan, J. Yang, W. Xu, P. An, S. Xi, J. Guo, B. Liu, J. Li, *Angew. Chem. Int. Ed.* **2022**, *61*, e202211031; *Angew. Chem.* **2022**, *134*, e202211031; d) Y. Pan, D. Li, H.-L. Jiang, *Chem. Eur. J.* **2018**, *24*, 18403.

[34] a) T. Zhou, Y. Du, A. Borgna, J. Hong, Y. Wang, J. Han, W. Zhang, R. Xu, *Energy Environ. Sci.* **2013**, *6*, 3229; b) S. Saha, G. Das, J. Thote, R. Banerjee, *J. Am. Chem. Soc.* **2014**, *136*, 14845–14851; c) J.-D. Xiao, Q. Shang, Y. Xiong, Q. Zhang, Y. Luo, S.-H. Yu, H.-L. Jiang, *Angew. Chem. Int. Ed.* **2016**, *55*, 9389–9393; *Angew. Chem.* **2016**, *128*, 9535–9539; d) D. Kim, D. R. Whang, S. Y. Park, *J. Am. Chem. Soc.* **2016**, *138*, 8698–8701.

[35] A. Cadiau, N. Kolobov, S. Srinivasan, M. G. Goesten, H. Haspel, A. V. Bavykina, M. R. Tchalala, P. Maity, A. Goryachev, A. S. Poryvaev, M. Eddaoudi, M. V. Fedin, O. F. Mohammed, J. Gascon, *Angew. Chem. Int. Ed.* **2020**, *59*, 13468–13472; *Angew. Chem.* **2020**, *132*, 13570–13574.

[36] B. Lerma-Berlanga, C. R. Ganivet, N. Almora-Barrios, S. Tatay, Y. Peng, J. Albero, O. Fabelo, J. González-Platas, H. García, N. M. Padial, C. Martí-Gastaldo, *J. Am. Chem. Soc.* **2021**, *143*, 1798–1806.

[37] T. F. Chen, L. Y. Wang, Y. F. Wang, H. Gao, J. He, G. Wang, X. F. Meng, Y. S. Wu, Y. H. Deng, C. Q. Wan, *ACS Appl. Mater. Interfaces* **2021**, *13*, 20897–20905.

[38] Y. Pan, J. Wang, S. Chen, W. Yang, C. Ding, A. Waseem, H.-L. Jiang, *Chem. Sci.* **2022**, *13*, 6696–6703.

[39] a) L. Shen, M. Luo, L. Huang, P. Feng, L. Wu, *Inorg. Chem.* **2015**, *54*, 1191–1193; b) C. Dong, C. Lian, S. Hu, Z. Deng, J. Gong, M. Li, H. Liu, M. Xing, J. Zhang, *Nat. Commun.* **2018**, *9*, 1252.

[40] C. Wang, K. E. deKrafft, W. Lin, *J. Am. Chem. Soc.* **2012**, *134*, 7211–7214.

[41] S. Li, H.-M. Mei, S.-L. Yao, Z.-Y. Chen, Y.-L. Lu, L. Zhang, C.-Y. Su, *Chem. Sci.* **2019**, *10*, 10577–10585.

[42] a) J. Ming, A. Liu, J. Zhao, P. Zhang, H. Huang, H. Lin, Z. Xu, X. Zhang, X. Wang, J. Hofkens, M. B. J. Roeffaers, J. Long, *Angew. Chem. Int. Ed.* **2019**, *58*, 18290–18294; *Angew. Chem.* **2019**, *131*, 18458–18462; b) M. Xu, D. Li, K. Sun, L. Jiao, C. Xie, C. Ding, H.-L. Jiang, *Angew. Chem. Int. Ed.* **2021**, *60*, 16372–16376; *Angew. Chem.* **2021**, *133*, 16508–16512.

[43] a) X. Fang, Q. Shang, Y. Wang, L. Jiao, T. Yao, Y. Li, Q. Zhang, Y. Luo, H.-L. Jiang, *Adv. Mater.* **2018**, *30*, 1705112; b) Q. Zuo, T. Liu, C. Chen, Y. Ji, X. Gong, Y. Mai, Y. Zhou, *Angew. Chem. Int. Ed.* **2019**, *58*, 10198–10203; *Angew. Chem.* **2019**, *131*, 10304–10309; c) T. He, S. Chen, B. Ni, Y. Gong, Z. Wu, L. Song, L. Gu, W. Hu, X. Wang, *Angew. Chem. Int. Ed.* **2018**, *57*, 3493–3498; *Angew. Chem.* **2018**, *130*, 3551–3556; d) H. Zhang, J. Wei, J. Dong, G. Liu, L. Shi, P. An, G. Zhao, J. Kong, X. Wang, X. Meng, J. Zhang, J. Ye, *Angew. Chem. Int. Ed.* **2016**, *55*, 14310–14314; *Angew. Chem.* **2016**, *128*, 14522–14526; e) X. Chen, S. Xiao, H. Wang, W. Wang, Y. Cai, G. Li, M. Qiao, J. Zhu, H. Li, D. Zhang, Y. Lu, *Angew. Chem. Int. Ed.* **2020**, *59*, 17182–17186; *Angew. Chem.* **2020**, *132*, 17335–17339; f) J. Sui, H. Liu, S. Hu, K. Sun, G. Wan, H. Zhou, X. Zheng, H.-L. Jiang, *Adv. Mater.* **2022**, *34*, 2109203.

[44] a) S. Pullen, H. Fei, A. Orthaber, S. M. Cohen, S. Ott, *J. Am. Chem. Soc.* **2013**, *135*, 16997–17003; b) K. Sasan, Q. Lin, C. Mao, P. Feng, *Chem. Commun.* **2014**, *50*, 10390–10393; c) W. Wang, X.-W. Song, Z. Hong, B. Li, Y. Si, C. Ji, K. Su, Y. Tan, Z. Ju, Y. Huang, C.-N. Chen, D. Yuan, *Appl. Catal. B* **2019**, *258*, 117979; d) M. A. Nasalevich, R. Becker, E. V. Ramos-Fernandez, S. Castellanos, S. L. Veber, M. V. Fedin, F. Kapteijn, J. N. H. Reek, J. I. van der Vlugt, J. Gascon, *Energy Environ. Sci.* **2015**, *8*, 364–375; e) Z. Li, J.-D. Xiao, H.-L. Jiang, *ACS Catal.* **2016**, *6*, 5359–5365; f) Y. Pi, X. Feng, Y. Song, Z. Xu, Z. Li, W. Lin, *J. Am. Chem. Soc.* **2020**, *142*, 10302–10307; g) X. Ma, H. Liu, W. Yang, G. Mao, L. Zheng, H.-L. Jiang, *J. Am. Chem. Soc.* **2021**, *143*, 12220–12229.

[45] a) A. W. Peters, Z. Li, O. K. Farha, J. T. Hupp, *ACS Appl. Mater. Interfaces* **2016**, *8*, 20675–20681; b) H. Zhao, Z. Jiang, K. Xiao, H. Sun, H. S. Chan, T. H. Tsang, S. Yang, P. K. Wong, *Appl. Catal. B* **2021**, *280*, 119456.

[46] a) S. Kampouri, T. N. Nguyen, C. P. Ireland, B. Valizadeh, F. M. Ebrahim, G. Capano, D. Ongari, A. Mace, N. Guijarro, K. Sivula, A. Sienkiewicz, L. Forró, B. Smit, K. C. Stylianou, *J. Mater. Chem. A* **2018**, *6*, 2476–2481; b) K. Sun, M. Liu, J. Pei, D. Li, C. Ding, K. Wu, H.-L. Jiang, *Angew. Chem. Int. Ed.* **2020**, *59*, 22749–22755; *Angew. Chem.* **2020**, *132*, 22937–22943; c) Y. Shi, B. Zhang, *Chem. Soc. Rev.* **2016**, *45*, 1529–1541.

[47] a) X. Y. Dong, M. Zhang, R. B. Pei, Q. Wang, D. H. Wei, S. Q. Zang, Y. T. Fan, T. C. Mak, *Angew. Chem. Int. Ed.* **2016**, *55*, 2073–2077; *Angew. Chem.* **2016**, *128*, 2113–2117; b) D. Shi, R. Zheng, M. J. Sun, X. Cao, C. X. Sun, C. J. Cui, C. S. Liu, J. Zhao, M. Du, *Angew. Chem. Int. Ed.* **2017**, *56*, 14637–14641; *Angew. Chem.* **2017**, *129*, 14829–14833; c) Y. Kamakura, P. Chinapang, S. Masaoka, A. Saeki, K. Ogasawara, S. R. Nishitani, H. Yoshikawa, T. Katayama, N. Tamai, K. Sugimoto, D. Tanaka, *J. Am. Chem. Soc.* **2020**, *142*, 27–32; d) L. Liu, S. Du, X. Guo, Y. Xiao, Z. Yin, N. Yang, Y. Bao, X. Zhu, S. Jin, Z. Feng, F. Zhang, *J. Am. Chem. Soc.* **2022**, *144*, 2747–2754.

[48] a) G. Paille, M. Gomez-Mingot, C. Roch-Marchal, B. Lassalle-Kaiser, P. Mialane, M. Fontecave, C. Mellot-Draznieks, A. Dolbecq, *J. Am. Chem. Soc.* **2018**, *140*, 3613–3618; b) W. A. Shah, A. Waseem, M. A. Nadeem, P. Kögerler, *Appl. Catal. A* **2018**, *567*, 132–138; c) Y. Horiuchi, T. Toyao, K. Miyahara, L. Zakary, D. D. Van, Y. Kamata, T. H. Kim, S. W. Lee, M. Matsuoka, *Chem. Commun.* **2016**, *52*, 5190–5193; d) L. Chi, Q. Xu, X. Liang, J. Wang, X. Su, *Small* **2016**, *12*, 1351–1358; e) N.-Y. Huang, J.-Q. Shen, Z.-M. Ye, W.-X. Zhang, P.-Q. Liao, X.-M. Chen, *Chem. Sci.* **2019**, *10*, 9859–9864; f) L. Li, Z.-B. Fang, W. Deng, J.-D. Yi, R. Wang, T.-F. Liu, *CCS Chem.* **2022**, *4*, 2782–2792.

[49] a) Y. An, Y. Liu, P. An, J. Dong, B. Xu, Y. Dai, X. Qin, X. Zhang, M. H. Whangbo, B. Huang, *Angew. Chem. Int. Ed.* **2017**, *56*, 3036–3040; *Angew. Chem.* **2017**, *129*, 3082–3086; b) S. Remiro-Buenamañana, M. Cabrero-Antonino, M. Martinez-Guanter, M. Alvaro, S. Navalon, H. Garcia, *Appl. Catal. B* **2019**, *254*, 677–684; c) J. Zhang, T. Bai, H. Huang, M.-H. Yu, X. Fan, Z. Chang, X.-H. Bu, *Adv. Mater.* **2020**, *32*, 2004747; d) A. Melillo, M. Cabrero-Antonino, S. Navalon, M. Alvaro, B. Ferrer, H. Garcia, *Appl. Catal. B* **2020**, *278*, 119345; e) P. Salcedo-Abraira, A. A. Babaryk, E. Montero-Lanzuela, O. R. Contreras-Almengor, M. Cabrero-Antonino, E. S. Grape, T. Willhammar, S. Navalon, E. Elkaim, H. Garcia, P. Horcajada, *Adv. Mater.* **2021**, *33*, 2106627; f) H. Hu, Z. Wang, L. Cao, L. Zeng, C. Zhang, W. Lin, C. Wang, *Nat. Chem.* **2021**, *13*, 358–366.

[50] a) M. Ding, R. W. Flaig, H.-L. Jiang, O. M. Yaghi, *Chem. Soc. Rev.* **2019**, *48*, 2783–2828; b) W. Fan, X. Zhang, Z. Kang, X. Liu, D. Sun, *Coord. Chem. Rev.* **2021**, *443*, 213968; c) J.-B. Lin, T. T. T. Nguyen, R. Vaidhyanathan, J. Burner, J. M. Taylor, H. Durekova, F. Akhtar, R. K. Mah, O. Ghaffari-Nik, S. Marx, N. Fylstra, S. S. Iremonger, K. W. Dawson, P. Sarkar, P. Hovington, A. Rajendran, T. K. Woo, G. K. H. Shimizu, *Science* **2021**, *374*, 1464–1469.

[51] a) K. E. Dalle, J. Warnan, J. J. Leung, B. Reuillard, I. S. Karmel, E. Reisner, *Chem. Rev.* **2019**, *119*, 2752–2875; b) H. Rao, L. C. Schmidt, J. Bonin, M. Robert, *Nature* **2017**, *548*, 74–77.

[52] a) C. Wang, Z. Xie, K. E. deKrafft, W. Lin, *J. Am. Chem. Soc.* **2011**, *133*, 13445–13454; b) H. Fei, M. D. Sampson, Y. Lee, C. P. Kubiak, S. M. Cohen, *Inorg. Chem.* **2015**, *54*, 6821–6828; c) U. J. Ryu, S. J. Kim, H. K. Lim, H. Kim, K. M. Choi, J. K. Kang, *Sci. Rep.* **2017**, *7*, 612; d) X. Feng, Y. Pi, Y. Song, C. Brzezinski, Z. Xu, Z. Li, W. Lin, *J. Am. Chem. Soc.* **2020**, *142*, 690–695; e) T.-C. Zhuo, Y. Song, G.-L. Zhuang, L.-P. Chang, S. Yao, W. Zhang, Y. Wang, P. Wang, W. Lin, T.-B. Lu, Z.-M. Zhang, *J. Am. Chem. Soc.* **2021**, *143*, 6114–6122; f) P. M. Stanley, J. Haimerl, C. Thomas, A. Urstoeger, M. Schuster, N. B. Shustova, A. Casini, B. Rieger, J. Warnan, R. A. Fischer, *Angew. Chem. Int. Ed.* **2021**, *60*, 17854–17860; *Angew. Chem.* **2021**, *133*, 17998–18004; g) N.-Y. Huang, H. He, S. Liu, H.-L. Zhu, Y.-J. Li, J. Xu, J.-R. Huang, X. Wang, P.-Q. Liao, X.-M. Chen, *J. Am. Chem. Soc.* **2021**, *143*, 17424–17430.

[53] a) K. M. Choi, D. Kim, B. Rungtaweevoranit, C. A. Trickett, J. T. Barmanbek, A. S. Alshammari, P. Yang, O. M. Yaghi, *J. Am. Chem. Soc.* **2017**, *139*, 356–362; b) L.-Y. Wu, Y.-F. Mu, X.-X. Guo, W. Zhang, Z.-M. Zhang, M. Zhang, T.-B. Lu, *Angew. Chem. Int. Ed.* **2019**, *58*, 9491–9495; *Angew. Chem.* **2019**, *131*, 9591–9595; c) R. Li, J. Hu, M. Deng, H. Wang, X. Wang, Y. Hu, H.-L. Jiang, J. Jiang, Q. Zhang, Y. Xie, Y. Xiong, *Adv. Mater.* **2014**, *26*, 4783–4788; d) Z. Jiang, X. Xu, Y. Ma, H. S. Cho, D. Ding, C. Wang, J. Wu, P. Oleynikov, M. Jia, J. Cheng, Y. Zhou, O. Terasaki, T. Peng, L. Zan, H. Deng, *Nature* **2020**, *586*, 549–554; e) J.-W. Wang, L.-Z. Qiao, H.-D. Nie, H.-H. Huang, Y. Li, S. Yao, M. Liu, Z.-M. Zhang, Z.-H. Kang, T.-B. Lu, *Nat. Commun.* **2021**, *12*, 813; f) Y. Chen, P. Li, J. Zhou, C. T. Buru, L. Đorđević, P. Li, X. Zhang, M. M. Cetin, J. F. Stoddart, S. I. Stupp, M. R. Wasielewski, O. K. Farha, *J. Am. Chem. Soc.* **2020**, *142*, 1768–1773.

[54] Y. Fu, D. Sun, Y. Chen, R. Huang, Z. Ding, X. Fu, Z. Li, *Angew. Chem. Int. Ed.* **2012**, *51*, 3364–3367; *Angew. Chem.* **2012**, *124*, 3420–3423.

[55] H.-Q. Xu, J. Hu, D. Wang, Z. Li, Q. Zhang, Y. Luo, S.-H. Yu, H.-L. Jiang, *J. Am. Chem. Soc.* **2015**, *137*, 13440–13443.

[56] a) S. Wang, W. Yao, J. Lin, Z. Ding, X. Wang, *Angew. Chem. Int. Ed.* **2014**, *53*, 1034–1038; *Angew. Chem.* **2014**, *126*, 1052–1056; b) D. Chen, H. Xing, C. Wang, Z. Su, *J. Mater. Chem. A* **2016**, *4*, 2657–2662; c) D. Wang, R. Huang, W. Liu, D. Sun, Z. Li, *ACS Catal.* **2014**, *4*, 4254–4260.

[57] a) W. Yang, H.-J. Wang, R.-R. Liu, J.-W. Wang, C. Zhang, C. Li, D.-C. Zhong, T.-B. Lu, *Angew. Chem. Int. Ed.* **2021**, *60*, 409–414; *Angew. Chem.* **2021**, *133*, 413–418; b) F. Guo, M.

Yang, R.-X. Li, Z.-Z. He, Y. Wang, W.-Y. Sun, *ACS Catal.* **2022**, *12*, 9486–9493.
[58] a) B. Tang, F.-X. Xiao, *ACS Catal.* **2022**, *12*, 9023–9057; b) J. Albero, Y. Peng, H. García, *ACS Catal.* **2020**, *10*, 5734–5749.
[59] a) Y. Liu, Y. Yang, Q. Sun, Z. Wang, B. Huang, Y. Dai, X. Qin, X. Zhang, *ACS Appl. Mater. Interfaces* **2013**, *5*, 7654–7658; b) J. Li, H. Huang, W. Xue, K. Sun, X. Song, C. Wu, L. Nie, Y. Li, C. Liu, Y. Pan, H.-L. Jiang, D. Mei, C. Zhong, *Nat. Catal.* **2021**, *4*, 719–729; c) G. Wang, C. T. He, R. Huang, J. Mao, D. Wang, Y. Li, *J. Am. Chem. Soc.* **2020**, *142*, 19339–19345; d) F. Yu, X. Jing, Y. Wang, M. Sun, C. Duan, *Angew. Chem. Int. Ed.* **2021**, *60*, 24849–24853; *Angew. Chem.* **2021**, *133*, 25053–25057; e) Z. B. Fang, T. T. Liu, J. Liu, S. Jin, X. P. Wu, X. Q. Gong, K. Wang, Q. Yin, T. F. Liu, R. Cao, H.-C. Zhou, *J. Am. Chem. Soc.* **2020**, *142*, 12515–12523; f) H. Wu, X. Y. Kong, X. Wen, S. P. Chai, E. C. Lovell, J. Tang, Y. H. Ng, *Angew. Chem. Int. Ed.* **2021**, *60*, 8455–8459; *Angew. Chem.* **2021**, *133*, 8536–8540.
[60] D. Gao, R. M. Arán-Ais, H. S. Jeon, B. Roldan Cuenya, *Nat. Catal.* **2019**, *2*, 198–210.
[61] a) D. U. Nielsen, X.-M. Hu, K. Daasbjerg, T. Skrydstrup, *Nat. Catal.* **2018**, *1*, 244–254; b) J.-B. Peng, H.-Q. Geng, X.-F. Wu, *Chem* **2019**, *5*, 526–552.
[62] a) K. Niu, Y. Xu, H. Wang, R. Ye, H. L. Xin, F. Lin, C. Tian, Y. Lum, K. C. Bustillo, M. M. Doeff, M. T. M. Koper, J. Ager, R. Xu, H. Zheng, *Sci. Adv.* **2017**, *3*, e1700921; b) S. Fu, S. Yao, S. Guo, G.-C. Guo, W. Yuan, T.-B. Lu, Z.-M. Zhang, *J. Am. Chem. Soc.* **2021**, *143*, 20792–20801; c) Y. S. Xia, M. Tang, L. Zhang, J. Liu, C. Jiang, G. K. Gao, L.-Z. Dong, L.-G. Xie, Y.-Q. Lan, *Nat. Commun.* **2022**, *13*, 2964.
[63] a) M. Dong, J.-X. Gu, C.-Y. Sun, X.-L. Wang, Z.-M. Su, *Chem. Commun.* **2022**, *58*, 10114–10126; b) T. Kajiwara, M. Fujii, M. Tsujimoto, K. Kobayashi, M. Higuchi, K. Tanaka, S. Kitagawa, *Angew. Chem. Int. Ed.* **2016**, *55*, 2697–2700; *Angew. Chem.* **2016**, *128*, 2747–2750; c) Y. Ma, Q. Tang, W.-Y. Sun, Z.-Y. Yao, W. Zhu, T. Li, J. Wang, *Appl. Catal. B* **2020**, *270*, 118856; d) B. Han, X. Ou, Z. Deng, Y. Song, C. Tian, H. Deng, Y. J. Xu, Z. Lin, *Angew. Chem. Int. Ed.* **2018**, *57*, 16811–16815; *Angew. Chem.* **2018**, *130*, 17053–17057; e) Y. Wang, N.-Y. Huang, J.-Q. Shen, P.-Q. Liao, X.-M. Chen, J.-P. Zhang, *J. Am. Chem. Soc.* **2018**, *140*, 38–41.
[64] H.-N. Wang, Y.-H. Zou, H.-X. Sun, Y. Chen, S.-L. Li, Y.-Q. Lan, *Coord. Chem. Rev.* **2021**, *438*, 213906.
[65] A. Olivo, E. Ghedini, M. Signoretto, M. Compagnoni, I. Rossetti, *Energies* **2017**, *10*, 1394.
[66] a) S.-M. Liu, Z. Zhang, X. Li, H. Jia, M. Ren, S. Liu, *Adv. Mater. Interfaces* **2018**, *5*, 1801062; b) W. Y. Gao, H. T. Ngo, Z. Niu, W. Zhang, Y. Pan, Z. Yang, V. R. Bhethanabotla, B. Joseph, B. Aguila, S. Ma, *ChemSusChem* **2020**, *13*, 6273–6277; c) J.-H. Qin, P. Xu, Y.-D. Huang, L.-Y. Xiao, W. Lu, X.-G. Yang, L.-F. Ma, S.-Q. Zang, *Chem. Commun.* **2021**, *57*, 8468–8471.
[67] a) Y. Su, Z. Zhang, H. Liu, Y. Wang, *Appl. Catal. B* **2017**, *200*, 448–457; b) N.-Y. Huang, J.-Q. Shen, X.-W. Zhang, P.-Q. Liao, J.-P. Zhang, X.-M. Chen, *J. Am. Chem. Soc.* **2022**, *144*, 8676–8682; c) L.-Z. Dong, L. Zhang, J. Liu, Q. Huang, M. Lu, W.-X. Ji, Y.-Q. Lan, *Angew. Chem. Int. Ed.* **2020**, *59*, 2659–2663; *Angew. Chem.* **2020**, *132*, 2681–2685; d) G. Lan, Y. Fan, W. Shi, E. You, S. S. Veroneau, W. Lin, *Nat. Catal.* **2022**, *5*, 1006–1018.
[68] a) L. Zhang, J. Ran, S. Z. Qiao, M. Jaroniec, *Chem. Soc. Rev.* **2019**, *48*, 5184–5206; b) Y. Gao, W. Nie, X. Wang, F. Fan, C. Li, *Chem. Commun.* **2020**, *56*, 1007–1021; c) T. J. Miao, J. Tang, *J. Chem. Phys.* **2020**, *152*, 194201.
[69] a) L. Hanna, P. Kucheryavy, C. Liu, X. Zhang, J. V. Lockard, *J. Phys. Chem. C* **2017**, *121*, 13570–13576; b) S. Yang, B. Pattengale, S. Lee, J. Huang, *ACS Energy Lett.* **2018**, *3*, 532–539; c) B. Pattengale, S. Yang, J. Ludwig, Z. Huang, X. Zhang, J. Huang, *J. Am. Chem. Soc.* **2016**, *138*, 8072–8075.
[70] a) R. Chen, F. Fan, C. Li, *Angew. Chem. Int. Ed.* **2022**, *61*, e202117567; *Angew. Chem.* **2022**, *134*, e202117567; b) Y. Liu, C. Chen, J. Valdez, D. Motta Meira, W. He, Y. Wang, C. Harnagea, Q. Lu, T. Guner, H. Wang, C.-H. Liu, Q. Zhang, S. Huang, A. Yurtsever, M. Chaker, D. Ma, *Nat. Commun.* **2021**, *12*, 1231; c) J. Li, Z. Cui, Y. Zheng, X. Liu, Z. Li, H. Jiang, S. Zhu, Y. Zhang, P. K. Chu, S. Wu, *Appl. Catal. B* **2022**, *317*, 121701.
[71] F. Zaera, *Chem. Soc. Rev.* **2014**, *43*, 7624–7663.
[72] a) A. J. Howarth, A. W. Peters, N. A. Vermeulen, T. C. Wang, J. T. Hupp, O. K. Farha, *Chem. Mater.* **2017**, *29*, 26–39; b) J. Gascon, M. D. Hernandez-Alonso, A. R. Almeida, G. P. van Klink, F. Kapteijn, G. Mul, *ChemSusChem* **2008**, *1*, 981–983; c) L. Li, Y. Li, L. Jiao, X. Liu, Z. Ma, Y.-J. Zeng, X. Zheng, H.-L. Jiang, *J. Am. Chem. Soc.* **2022**, *144*, 17075–17085; d) S. Karmakar, S. Barman, F. A. Rahimi, T. K. Maji, *Energy Environ. Sci.* **2021**, *14*, 2429–2440; e) S. Kattel, B. Yan, Y. Yang, J. G. Chen, P. Liu, *J. Am. Chem. Soc.* **2016**, *138*, 12440–12450.
[73] a) S. A. Bonke, T. Risse, A. Schnegg, A. Brückner, *Nat. Rev. Methods Primers* **2021**, *1*, 33; b) T. Biskup, *Front. Chem.* **2019**, *7*, 10.
[74] a) Z.-H. Yan, M.-H. Du, J. Liu, S. Jin, C. Wang, G.-L. Zhuang, X.-J. Kong, L.-S. Long, L.-S. Zheng, *Nat. Commun.* **2018**, *9*, 3353; b) P. Karthik, R. Vinoth, P. Zhang, W. Choi, E. Balaraman, B. Neppolian, *ACS Appl. Energy Mater.* **2018**, *1*, 1913–1923.
[75] a) L. Nguyen, F. F. Tao, Y. Tang, J. Dou, X.-J. Bao, *Chem. Rev.* **2019**, *119*, 6822–6905; b) M. Zhang, M. Lu, Z.-L. Lang, J. Liu, M. Liu, J.-N. Chang, L.-Y. Li, L.-J. Shang, M. Wang, S.-L. Li, Y.-Q. Lan, *Angew. Chem. Int. Ed.* **2020**, *59*, 6500–6506; *Angew. Chem.* **2020**, *132*, 6562–6568; c) J. Wang, Y. Mao, R. Zhang, Y. Zeng, C. Li, B. Zhang, J. Zhu, J. Ji, D. Liu, R. Gao, Y. Ma, *Adv. Sci.* **2022**, *9*, 2204036; d) L. Zhang, R. Long, Y. Zhang, D. Duan, Y. Xiong, Y. Zhang, Y. Bi, *Angew. Chem. Int. Ed.* **2020**, *59*, 6224–6229; *Angew. Chem.* **2020**, *132*, 6283–6288.
[76] Z. Wang, T. Hisatomi, R. Li, K. Sayama, G. Liu, K. Domen, C. Li, L. Wang, *Joule* **2021**, *5*, 344–359.
[77] C. Zhang, D. Lei, C. Xie, X. Hang, C. He, H.-L. Jiang, *Adv. Mater.* **2021**, *33*, 2106308.
[78] D. Mateo, A. Santiago-Portillo, J. Albero, S. Navalón, M. Alvaro, H. García, *Angew. Chem. Int. Ed.* **2019**, *58*, 17843; *Angew. Chem.* **2019**, *131*, 18007.
[79] a) J. Hong, W. Zhang, J. Ren, R. Xu, *Anal. Methods* **2013**, *5*, 1086–1097; b) R. Das, S. Chakraborty, S. C. Peter, *ACS Energy Lett.* **2021**, *6*, 3270–3274.
[80] F. Xu, K. Meng, B. Cheng, S. Wang, J. Xu, J. Yu, *Nat. Commun.* **2020**, *11*, 4613.
[81] D. E. Henton, C. Powell, R. E. Reim, *J. Appl. Polym. Sci.* **1997**, *64*, 591–600.
[82] D. Zhang, Y. Zhu, L. Liu, X. Ying, C.-E. Hsiung, R. Sougrat, K. Li, Y. Han, *Science* **2018**, *359*, 675–679.
[83] J. Nyakuchena, S. Ostresh, D. Streater, B. Pattengale, J. Neu, C. Fiankor, W. Hu, E. D. Kinigstein, J. Zhang, X. Zhang, C. A. Schmuttenmaer, J. Huang, *J. Am. Chem. Soc.* **2020**, *142*, 21050–21058.
[84] Y. Wang, H. Lv, E. S. Grape, C. A. Gaggioli, A. Tayal, A. Dharanipragada, T. Willhammar, A. K. Inge, X. Zou, B. Liu, Z. Huang, *J. Am. Chem. Soc.* **2021**, *143*, 6333–6338.
[85] A. Schneemann, V. Bon, I. Schwedler, I. Senkovska, S. Kaskel, R. A. Fischer, *Chem. Soc. Rev.* **2014**, *43*, 6062–6096.
[86] L. Jiao, J. Wang, H.-L. Jiang, *Acc. Mater. Res.* **2021**, *2*, 327–339.

[87] S. M. Moosavi, A. Nandy, K. M. Jablonka, D. Ongari, J. P. Janet, P. G. Boyd, Y. Lee, B. Smit, H. J. Kulik, *Nat. Commun.* **2020**, *11*, 4068.
[88] Q. Huang, J. Liu, L. Feng, Q. Wang, W. Guan, L.-Z. Dong, L. Zhang, L.-K. Yan, Y.-Q. Lan, H.-C. Zhou, *Natl. Sci. Rev.* **2020**, *7*, 53–63.
[89] X. Chen, C. Peng, W. Dan, L. Yu, Y. Wu, H. Fei, *Nat. Commun.* **2022**, *13*, 4592.
[90] P. G. Boyd, A. Chidambaram, E. Garcia-Diez, C. P. Ireland, T. D. Daff, R. Bounds, A. Gladysiak, P. Schouwink, S. M. Moosavi, M. M. Maroto-Valer, J. A. Reimer, J. A. R. Navarro, T. K. Woo, S. Garcia, K. C. Stylianou, B. Smit, *Nature* **2019**, *576*, 253–256.
[91] a) L.-L. Ling, W. Yang, P. Yan, M. Wang, H.-L. Jiang, *Angew. Chem. Int. Ed.* **2022**, *61*, e202116396; *Angew. Chem.* **2022**, *134*, e202116396; b) Y.-Z. Chen, Z. U. Wang, H. Wang, J. Lu, S.-H. Yu, H.-L. Jiang, *J. Am. Chem. Soc.* **2017**, *139*, 2035–2044; c) Q. Yang, Q. Xu, S.-H. Yu, H.-L. Jiang, *Angew. Chem. Int. Ed.* **2016**, *55*, 3685–3689; *Angew. Chem.* **2016**, *128*, 3749–3753; d) Q. Yang, C.-C. Yang, C.-H. Lin, H.-L. Jiang, *Angew. Chem. Int. Ed.* **2019**, *58*, 3511–3515; *Angew. Chem.* **2019**, *131*, 3549–3553.
[92] a) S. Kampouri, K. C. Stylianou, *ACS Catal.* **2019**, *9*, 4247–4270; b) H. Liu, C. Xu, D. Li, H.-L. Jiang, *Angew. Chem. Int. Ed.* **2018**, *57*, 5379–5383; *Angew. Chem.* **2018**, *130*, 5477–5481.

Manuscript received: November 29, 2022
Accepted manuscript online: January 23, 2023
Version of record online: February 6, 2023